

Origin of Fe³⁺ in Fe-containing, Al-free Mantle Silicate Perovskite

Shenzhen Xu¹, Sang-Heon Shim³, Dane Morgan^{1,2}

¹*Materials Science Program*

²*Department of Materials Science and Engineering
University of Wisconsin – Madison, Madison, WI*

³*School of Earth and Space Exploration
Arizona State University, Tempe, AZ*

Corresponding author: Telephone: +1-608-265-5879; Fax: +1-608-262-8353; Email:
ddmorgan@wisc.edu

Abstract

We have studied the ferrous (Fe²⁺) and ferric (Fe³⁺) iron concentrations in Al-free Fe containing Mg-silicate perovskite (Mg-Pv) at pressure (P), temperature (T), and oxygen fugacity (fO_2) conditions related to the lower mantle using a thermodynamic model based on ab-initio calculations. We consider the oxidation reaction and the charge disproportionation reaction, both of which can produce Fe³⁺ in Mg-Pv. The model shows qualitatively good agreement with available experimental data on Fe³⁺/ΣFe (ΣFe = total Fe in system), spin transitions, and equations of state. We predict that under lower-mantle conditions Fe³⁺/ΣFe determined by the charge disproportionation is estimated to be 0.01-0.07 in Al-free Mg-Pv, suggesting that low Al Mg-Pv in the uppermost pyrolitic mantle (where majoritic garnet contains most of the Al) and in the harzburgitic heterogeneities throughout the lower mantle contains very little Fe³⁺. We find that the volume reduction by the spin transition of the B-site Fe³⁺ leads to a minimum Fe³⁺/ΣFe in Mg-Pv at mid-mantle pressures. The model shows that configurational entropy is a key driving force to create Fe³⁺ and therefore Fe³⁺ content is highly temperature sensitive. The temperature sensitivity may lead to a maximum Fe³⁺/ΣFe in Mg-Pv in warm regions at the core-mantle boundary region, such as Large Low Shear Velocity Provinces (LLSVPs), potentially altering the physical (e.g., bulk modulus) and transport (e.g., thermal and electrical conductivities) properties of the heterogeneities.

1. Introduction

Mg-silicate perovskite (Mg-Pv, bridgmanite) is the most abundant mineral phase in the lower mantle of the Earth. More than 70 percent of the lower mantle may be made up of Mg-Pv by volume and iron is the most abundant transition metal element in the lower mantle (Irifune et al., 2010). Iron is known to exist in Mg-Pv as both Fe^{2+} and Fe^{3+} (McCammon, 1997; Frost et al., 2004). The presence of Fe^{3+} can influence a number of physical and chemical properties of Mg-Pv. For example, the high spin to low spin transition of Fe^{3+} in the B-site of Mg-Pv may cause an anomalous behavior of the bulk modulus affecting Mg-Pv mechanical behavior (Hsu et al., 2011). This spin transition of Fe^{3+} may also lead to a volume collapse and increase the density (Catalli et al., 2011, 2010; Hsu et al., 2011). Moreover an increase in the Fe^{3+} concentration has been shown to increase the electrical conductivity (McCammon, 1997) and radiative thermal conductivity (Goncharov et al., 2008) of Mg-Pv. Many experiments have shown that even if the starting materials do not contain any Fe^{3+} , Mg-Pv synthesized at lower mantle pressures-temperature (P - T) conditions contains Fe^{3+} (Frost and Langenhorst, 2002; Sinmyo et al., 2008; Grocholski et al., 2009). The Fe^{3+} concentration in Mg-Pv ($[\text{Fe}^{3+}]/([\text{Fe}^{2+}] + [\text{Fe}^{3+}]) = \text{Fe}^{3+}/\Sigma\text{Fe}$, where $[X]$ is the number of moles of X ranges from 0.1 to 0.6. Furthermore, the amount of Fe^{3+} is very different between Al-free and Al-bearing Mg-Pv (Frost et al., 2004; McCammon et al., 2004; Nakajima et al., 2012), with Al bearing Mg-Pv containing much more Fe^{3+} .

Two mechanisms have been considered to dominate the formation of Fe^{3+} in Mg-Pv (Frost et al., 2004; Nakajima et al., 2012; Zhang and Oganov, 2006): (a) the oxidation reaction, where Fe^{2+} is oxidized to Fe^{3+} under elevated oxygen fugacity ($f\text{O}_2$), and (b) the charge disproportionation (chg. disp.) reaction, where Fe spontaneously disproportionates through $3\text{Fe}^{2+} \Rightarrow 2\text{Fe}^{3+} + \text{Fe}^0$. The oxidation reactions in our work are written in terms of a reaction with O_2 gas with a specific $f\text{O}_2$. This approach avoids the complexity of tracking all the possible reduction reactions that might release oxygen from the oxide phases as we simply represent their combined contribution to the environment by O_2 gas with a given $f\text{O}_2$. This approach also has the advantage of providing a common reference

for the oxidative strength of the environment that can be used to consider different conditions. However, we note that under lower mantle conditions it is expected that essentially all the oxygen is stored in solid phases and any significant reactions incorporating oxygen will take place through reduction and oxygen release of other oxide phases. As we will show below, under these conditions no excess oxygen is available for oxidation of Fe^{2+} , the $f\text{O}_2$ is very low, and only chg. disp. can change the $\text{Fe}^{3+}/\Sigma\text{Fe}$ ratio.

Because Fe^{3+} content may depend on $f\text{O}_2$, it is important to control $f\text{O}_2$ in experiments to the extent possible. In some cases, metallic iron powder was mixed with the starting material to ensure reducing conditions (Frost et al., 2004; Grocholski et al., 2009), although the exact $f\text{O}_2$ is still not known. In most diamond-anvil cell experiments, $f\text{O}_2$ has not been carefully regulated or characterized. Because of the limited sample chamber space in a multi-anvil press, the capsule materials have been used to control the $f\text{O}_2$ in the chamber, such as Re and diamond capsules (Lautherbach et al., 2000; Frost et al., 2004). In this work, we use the $f\text{O}_2$ of the capsule materials to approximate the $f\text{O}_2$ in the sample chamber (Nakajima et al., 2012) and the details of the determination of $f\text{O}_2$ at different T - P are shown in Supplemental information (SI) section 1.

The chg. disp. reaction has been studied in both experiments (Frost et al., 2004; McCammon, 1997) and simulations (Zhang and Oganov, 2006). Whereas the experiments suggest $\text{Fe}^{3+}/\Sigma\text{Fe} = 0\sim 0.3$ in Al-free Mg-Pv, the simulations imply spontaneous oxidation of all Fe to Fe^{3+} (and therefore $\text{Fe}^{3+}/\Sigma\text{Fe} \sim 1$) in Al-free Mg-Pv. Furthermore, a number of uncertainties remain about Fe^{3+} in Mg-Pv, including the extent to which each of the two mechanisms (oxidation reaction and chg. disp. reaction) contributes more to its formation, the balance of enthalpic and entropic driving forces governing Fe^{3+} formation (which will control the temperature dependence of the Fe^{3+} concentration), and what Fe^{3+} - $f\text{O}_2$ relationship exists at lower mantle P - T conditions, which are difficult to achieve in laboratory experiments. In this study we develop an ab-initio based thermodynamic model to understand and quantify the mechanisms that produce Fe^{3+} at high P - T . In our detailed models for generating Fe^{3+} in Mg-Pv we do not include any mechanisms involving creation of oxygen vacancies, although we do

consider the energetics of relevant reactions in section 2.1.1. There is still some debate about whether oxygen vacancy substitution plays a significant role when Fe^{3+} enters into the Mg-Pv and is evidence from previous experimental work (McCammon, 1998) suggesting that oxygen vacancy substitution may be the dominant mechanism in Al-free Mg-Pv. However, some previous experimental and simulation studies (Lauterbach et al., 2000; Frost et al., 2002; Brodholt et al., 2000; Zhang and Oganov, 2006) as well as our own calculations (see Eq. 2 in section 2.1.1) indicate that the charge-coupled substitution considered in this work is much more favorable than oxygen vacancy mechanisms under the lower mantle relevant conditions. In particular, in Zhang and Oganov's (Zhang and Oganov, 2006) work, they explicitly showed that oxygen vacancy substitution is unfavorable compared with charge-coupled substitution in Al-free Mg-Pv, which is consistent with our calculation in section 2.1.1. Given that we do not predict the oxygen vacancy substitution mechanism to be active we do not include the mechanism in our detailed thermodynamic models.

We focus on Al-free Mg-Pv in order to avoid the large increase in complexity associated with the presence of Al. This simpler model can help us understand the origin of Fe^{3+} and its dependence on different factors more easily than one containing Al. In addition, Al-free Mg-Pv is of interest for comparison to multiple Al free experiments as well as the upper part of the lower mantle and some subducting slabs, which are expected to have low Al concentration.

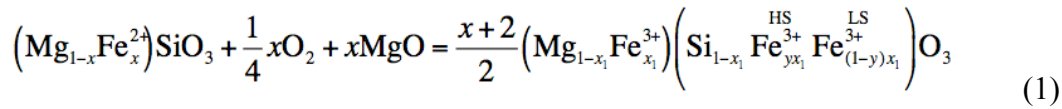
We will answer the following questions. (1) what are the dominant processes and thermodynamics driving forces that produce Fe^{3+} at experimental and lower mantle conditions, (2) what is the effect of spin transition, pressures and temperatures on Fe^{3+} concentration, and (3) what is the dependence of $\text{Fe}^{3+}/\Sigma\text{Fe}$ on $f\text{O}_2$ in Al-free Mg-Pv. The understanding of the thermodynamics of the Al-free Mg-Pv obtained from this work will guide researchers in building a more complete Al-bearing model in the future.

2. Modeling

2.1 Thermodynamic model

2.1.1 Oxidation model

The oxidation reaction occurs at a certain oxidation potential, which is represented by oxygen gas at a specific fO_2 . As noted in section 1, the use of O_2 gas to describe $\mu(O_2)$ is consistent with the fact that the oxygen in the lower mantle is stored in a solid form. We assume the oxidation reaction occurs via the charge-coupled substitution (Lauterbach et al., 2000; Frost et al., 2002; Zhang and Oganov, 2006) mechanism, where MgO is incorporated and Fe^{2+} is oxidized and substitutes on the B-site (see below for discussion of another other possible vacancy mediated oxidation reaction). The equation describing this oxidation reaction under conditions of excess MgO can be written:

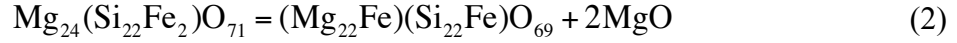


where $x_1 = x / (x+2)$, Fe^{HS} and Fe^{LS} refer to the high-spin and low-spin Fe respectively. The first term in the left hand side is ferrous Mg-Pv and x is the fraction of Fe in the A site. The right hand side material is ferric Mg-Pv. The total Fe content in Mg-Pv is approximately 0.1~0.2 in previous experimental and simulation studies and also in the lower mantle (Auzende et al., 2008; Frost et al., 2004; Hsu et al., 2011; Irifune et al., 2010; Mao et al., 2011b; Grocholski et al., 2009). In the following calculations we set $x = 0.125$. In most cases one is interested in Mg-Pv coexisting with ferropericlase (Mg,Fe)O and there will be Fe partitioning between the phases. This partitioning can change the content of Fe in the Mg-Pv but such changes turn out to have a minor effect on the $Fe^{3+}/\Sigma Fe$ ratio within the Mg-Pv in the Al-free case. The impact of the Fe partitioning on the $Fe^{3+}/\Sigma Fe$ in is discussed in SI section 4.

Some previous experimental and simulation studies showed that in the lower-mantle pressure range up to 130 GPa, there is a HS to LS transition for Fe on only the B-site Fe^{3+} (Bengtson et al., 2008; Catalli et al., 2010; Hsu et al., 2012, 2011; Lin et al., 2012). In Eq. (1), the parameter y gives the fraction of Fe^{3+} that is high spin in the B site.

In this work we do not include the production of Fe^{3+} by oxygen vacancy substitution in the models and we assume all the Fe^{3+} enters into Mg-Pv by charge-coupled substitution, as described in Eq. (1). Previous ab initio study of the Al^{3+} incorporation into the Mg-Pv

suggested that compared with charge-coupled substitution, oxygen vacancy substitution is unfavorable above 30 GPa (Brodholt, 2000), and here we demonstrate that this result holds for the ab initio methods used in this paper as well. Following the approach of Zhang and Oganov (2006), in order to evaluate whether oxygen vacancy substitution is favorable, we can study the following reaction:



It represents the reaction from an oxygen vacancy substitution to a charge coupled substitution. Our calculated reaction enthalpy ΔH is -6.23 eV at $P = 40$ GPa, which means the charge coupled substitution is much more stable than the oxygen vacancy substitution at lower-mantle conditions.

In order to model the free energies of reactions, the enthalpies are determined from ab initio calculations and the entropies are determined from analytical models.

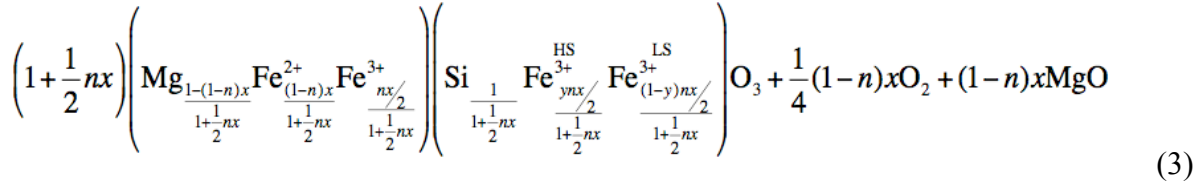
Configuration entropy is assumed to be ideal for all mixed occupation sublattices. The magnetic-electronic entropy is modeled based on totally disordered spins. It is assumed that the vibrational free energy of solid phase atoms cancels between reactants and products in Eq. (1) and the vibrational free energy difference between the O_2 gas and the O^{2-} ions of the solid is treated by applying an empirical thermodynamic free energy model for O_2 gas and a simple Einstein model (with Einstein temperature 500 K) for solid O^{2-} ions (Lee and Morgan, 2012). The empirical free energy expression for the oxygen

atom (gas phase) is: $\frac{1}{2}(H_{\text{O}_2}^{\text{NIST}} - TS_{\text{O}_2}^{\text{NIST}} + kT \ln f_{\text{O}_2})$. $(H_{\text{O}_2}^{\text{NIST}} - TS_{\text{O}_2}^{\text{NIST}})$ is the empirical free energy of O_2 at $P^0(\text{O}_2) = 1$ bar, referenced to $H_{\text{O}_2}^{\text{NIST}} (T = 298.15 \text{ K})$. $kT \ln f_{\text{O}_2}$ is the contribution to the oxygen free energy due to the change of $P(\text{O}_2)$ from the reference state of 1 atm. For the solid O^{2-} ions, the free energy based on a simple Einstein model is:

$(G_{\text{vib}}(\text{O}_{\text{solid}}^{2-}) - H_{\text{vib}}^0(\text{O}_{\text{solid}}^{2-}))$ with Einstein temperature = 500 K, which is referenced to $H_{\text{vib}}^0(\text{O}_{\text{solid}}^{2-}) (T = 298.15 \text{ K})$. The exact expressions and necessary parameters of all the terms above can be found in Lee and Morgan (2012). The energy correction term of O_2 due to the over-binding from DFT is very small in HSE06 (Chevrier et al., 2010) and can

be ignored. The fO_2 values at high P - T are extrapolated from experimental results (Campbell et al., 2007). Please see the details in the SI section 1.

To simplify the modeling, we write the whole system, both reactants and products in Eq. (1), in a compact form as



The parameter n gives the fraction of ferrous Mg-Pv transformed to ferric Mg-Pv. Note that it is assumed that the reactants and products can be mixed into the same Mg-Pv alloy, yielding multiple species on each Mg-Pv sublattice. In the thermodynamic model, we assume the impurity atoms on sub-lattices do not interact with each other. This assumption allows the enthalpy of the whole system to be written as a linear combination of its end-members. Writing the total Gibbs energy of the system in this way allows it to be expressed as a function of n and y at a given pressure and temperature as:

$$\begin{aligned} G_{TotalOx} = & (1-n)H[(\text{Mg}_{1-x}\text{Fe}_x)\text{SiO}_3] + \frac{x+2}{2}nyH[(\text{Mg}_{1-x_1}\text{Fe}_{x_1})\left(\text{Si}_{1-x_1}^{\text{HS}}\text{Fe}_{x_1}\right)\text{O}_3] + \frac{x+2}{2}n(1-y)H[(\text{Mg}_{1-x_1}\text{Fe}_{x_1})\left(\text{Si}_{1-x_1}^{\text{LS}}\text{Fe}_{x_1}\right)\text{O}_3] \\ & + \frac{1}{4}(1-n)x\mu(\text{O}_2) + (1-n)xH[\text{MgO}] - (1-n)xTS_{mag}(\text{Fe}^{2+}, A) - \frac{x+2}{2}nx_1TS_{mag}(\text{Fe}^{3+}, A) - \frac{x+2}{2}nyx_1TS_{mag}(\text{Fe}^{3+ \text{HS}}, B) - \\ & \frac{x+2}{2}n(1-y)x_1TS_{mag}(\text{Fe}^{3+ \text{LS}}, B) - (1 + \frac{1}{2}nx)TS_{conf}(A) - (1 + \frac{1}{2}nx)TS_{conf}(B) \end{aligned} \quad (4)$$

where $G_{TotalOx}$ is the total Gibbs energy for the system with states associated with this oxidation reaction. $S_{conf}(A)$ and $S_{conf}(B)$ are the configurational entropy from the A-site and B-site sublattices of Mg-Pv, respectively. The expressions for $S_{conf}(A)$ and $S_{conf}(B)$ are:

$$S_{conf}(A) = -k \left[\frac{1-(1-n)x}{1+\frac{1}{2}nx} \ln\left(\frac{1-(1-n)x}{1+\frac{1}{2}nx}\right) + \frac{(1-n)x}{1+\frac{1}{2}nx} \ln\left(\frac{(1-n)x}{1+\frac{1}{2}nx}\right) + \frac{nx/2}{1+\frac{1}{2}nx} \ln\left(\frac{nx/2}{1+\frac{1}{2}nx}\right) \right] \quad (5)$$

$$S_{conf}(B) = -k \left[\frac{1}{1 + \frac{1}{2}nx} \ln \left(\frac{1}{1 + \frac{1}{2}nx} \right) + \frac{\frac{ynx}{2}}{1 + \frac{1}{2}nx} \ln \left(\frac{\frac{ynx}{2}}{1 + \frac{1}{2}nx} \right) + \frac{\frac{(1-y)nx}{2}}{1 + \frac{1}{2}nx} \ln \left(\frac{\frac{(1-y)nx}{2}}{1 + \frac{1}{2}nx} \right) \right] \quad (6)$$

The $S_{mag}(Fe^{2+}, A)$, $S_{mag}(Fe^{3+}, A)$, $S_{mag}(Fe^{3+,HS}, B)$ and $S_{mag}(Fe^{3+,LS}, B)$ are the magnetic entropies of Fe^{2+} in the A site, Fe^{3+} in the A site, high spin Fe^{3+} in the B site and low spin Fe^{3+} in the B site, respectively. These values can be obtained by calculating the degeneracy of the electronic configuration of the d -orbital of Fe in different sites and spin states (Sturhahn, 2005; Tsuchiya et al., 2006). The expression for S_{mag} is $k_B \ln[m(2S+1)]$, where m is the electronic configuration degeneracy and S is the iron spin quantum number. The entropy values are given for each as (Sturhahn (2005); Zhang and Oganov (2006)):

$S_{mag}(Fe^{2+}, A)$	$S_{mag}(Fe^{3+}, A)$	$S_{mag}(Fe^{3+,HS}, B)$	$S_{mag}(Fe^{3+,LS}, B)$
$k_B \ln 10$	$k_B \ln 6$	$k_B \ln 6$	$k_B \ln 6$

The equilibrium B-site HS fraction (given by y) and Fe^{3+} fraction (given by n) can be predicted by minimizing the Gibbs free energy, which in general we will denote with G , with respect to n and y by solving the equations:

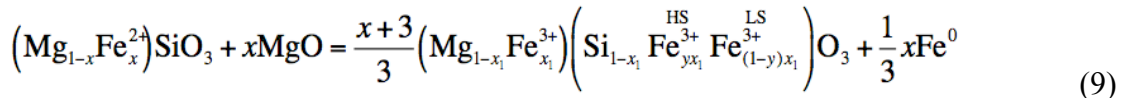
$$\begin{cases} \frac{\partial G(n, y; T, P)}{\partial n} = 0 \\ \frac{\partial G(n, y; T, P)}{\partial y} = 0 \end{cases} \quad (7)$$

2.1.2 Charge disproportionation

Chg. disp. reaction is a spontaneous valence state change of Fe^{2+} . The general expression for chg. disp. reaction is:



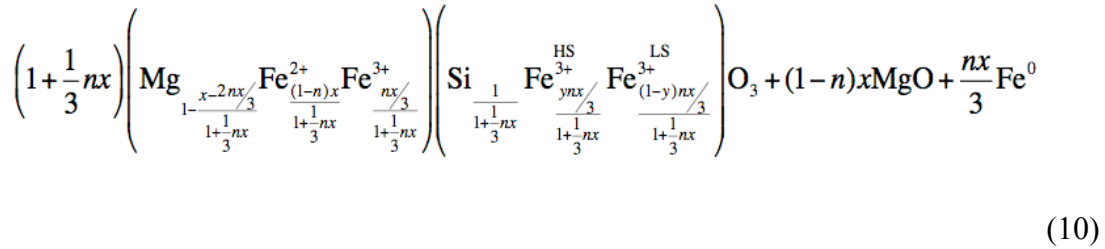
If there is only Fe^{2+} in the starting Mg-Pv material, Fe^{3+} can be produced by the chg. disp. reaction. The equation for this process in the presence of MgO is:



where $x_1 = x/(x+3)$. As above for the oxidation reaction, we take $x = 1/8$.

In both oxidation and chg. disp. reaction models, we always use the condition that MgO is excess. This choice is because: (1) in the lower mantle, the molar ratio of MgO/MgSiO₃ is about 0.6:1 (Irifune et al., 2010; Kesson et al., 1998; Mao, 1997), so the excess MgO amount is sufficient for the reactions, and (2) in many experiments the starting material is olivine (Mg,Fe)₂SiO₄, therefore the molar ratio of Fp/Mg-Pv, where Fp is ferropericclass, in these experiments is 1:1 (Auzende et al., 2008; Nakajima et al., 2012; Sinmyo et al., 2008), which again means there is sufficient excess MgO for the reactions.

We follow the same strategy used above for the oxidation reaction to find the Gibbs free energy of the system under the chg. disp. reaction. When a fraction n of the reactants in Eq. (9) are transferred to products, we can write the whole mixed system in the compact form:



From this expression we can write the total Gibbs energy of the system as:

$$\begin{aligned} G_{TotalChgDisp} = & (1-n)H[(\text{Mg}_{1-x}\text{Fe}_x)\text{SiO}_3] + \frac{x+3}{3}nyH[(\text{Mg}_{1-x_1}\text{Fe}_{x_1})\left(\text{Si}_{1-x_1}\text{Fe}_{x_1}^{\text{HS}}\right)\text{O}_3] + \frac{x+3}{3}n(1-y)H[(\text{Mg}_{1-x_1}\text{Fe}_{x_1})\left(\text{Si}_{1-x_1}\text{Fe}_{x_1}^{\text{LS}}\right)\text{O}_3] \\ & + (1-n)xH[\text{MgO}] + \frac{xn}{3}H[\text{Fe}] - (1-n)xTS_{mag}(\text{Fe}^{2+}, A) - \frac{x+3}{3}nx_1TS_{mag}(\text{Fe}^{3+}, A) - \frac{x+3}{3}nyx_1TS_{mag}(\text{Fe}^{3+\text{HS}}, B) - \\ & \frac{x+3}{3}n(1-y)x_1TS_{mag}(\text{Fe}^{3+\text{LS}}, B) - \frac{xn}{3}TS[\text{Fe}^0] - (1 + \frac{1}{3}nx)TS_{conf}(A) - (1 + \frac{1}{3}nx)TS_{conf}(B) \end{aligned} \quad (11)$$

where $G_{TotalChgDisp}$ is the total Gibbs energy for the system with states associated with this chg. disp. reaction. Parallel to the oxidation reaction case, we can solve Eq. (7) to find the extent of Fe²⁺ formation (from chg. disp. reaction) n and the B-site HS fraction y as a function of pressure and temperature.

The terms in Eq. (11) are found following the same approach and approximations as described for the oxidation reaction, except that now we must determine the entropy of metallic Fe. For the entropy of metallic Fe we include only magnetic contributions, consistent with the analysis in the oxide phases, and use the theoretical result from the Sommerfeld expansion (Ashcroft and Mermin, 1976),

$$S = \frac{\pi^2 D(E_F)}{3} k_B^2 T \quad (12)$$

where $D(E_F)$ is the density of states of metallic Fe at Fermi level. We get the $D(E_F)$ as a function of pressure from HSE06 hybrid DFT calculation for non-magnetic hexagonal close packed (hcp) Fe from 20 to 120 GPa.

2.1.3 Integrated model

In this section we combine the oxidation reaction model and chg. disp. reaction model together. The approach is the same as with the previous models treated separately. Consider the equilibration process by starting with one mole of $(\text{Mg}_{1-x}\text{Fe}_x)\text{SiO}_3$. When the system comes into equilibrium, n_1 mole of ferrous Mg-Pv is transferred to ferric Mg-Pv through the oxidation reaction and n_2 mole of ferrous Mg-Pv is transferred to ferric Mg-Pv through the chg. disp. reaction. Then the compact form for the whole system is:

$$\left(1 + \frac{1}{2}n_1x + \frac{1}{3}n_2x\right) \left(\text{Mg}_{\frac{1-(1-n_1-n_2)x}{1+\frac{1}{2}n_1x+\frac{1}{3}n_2x}} \text{Fe}_{\frac{(1-n_1-n_2)x}{1+\frac{1}{2}n_1x+\frac{1}{3}n_2x}}^{2+} \text{Fe}_{\frac{n_1x/2+n_2x/3}{1+\frac{1}{2}n_1x+\frac{1}{3}n_2x}}^{3+} \right) \left(\text{Si}_{\frac{1}{1+\frac{1}{2}n_1x+\frac{1}{3}n_2x}} \text{Fe}_{\frac{y(n_1x/2+n_2x/3)}{1+\frac{1}{2}n_1x+\frac{1}{3}n_2x}}^{\text{HS } 3+} \text{Fe}_{\frac{(1-y)(n_1x/2+n_2x/3)}{1+\frac{1}{2}n_1x+\frac{1}{3}n_2x}}^{\text{LS } 3+} \right) \text{O}_3 + \frac{1}{4}(1-n_1)x\text{O}_2 + (1-n_1-n_2)x\text{MgO} + \frac{n_2x}{3}\text{Fe}^0 \quad (13)$$

The further details of the Gibbs energy expressions are discussed in the SI section 2.

2.2 DFT methods

Our ab-initio calculations are performed with the Vienna ab initio simulation package (VASP) based on density functional theory. Projector augmented wave method (PAW) (Blochl, 1994) is used for the effective potential for all the atoms in the system. The

PAW potentials we use have $2p^63s^2$ for Mg, $3s^23p^2$ for Si, $2s^22p^4$ for O and $3p^63d^74s^1$ for Fe. A 600 eV energy cutoff is used to make sure the plane wave basis is large enough for converged calculations.

As there are transition metal atoms (Fe) in the system, the normal Local Density Approximation (LDA) and Generalized Gradient Approximation (GGA) functionals often provide inaccurate energetics (Wang et al., 2006). All the calculations in this work are therefore performed with HSE06 hybrid functional (Heyd et al., 2006, 2003; Paier et al., 2006) as implemented in the VASP code. The HSE06 functional has been shown to yield significantly more accurate energetics for transition metal redox reactions than standard LDA or GGA techniques (Chevrier et al., 2010). More quantitatively, Chevrier, et al. (2010) showed that the root mean squared error compared to experiment for a large series of transition metal oxidation reactions is 75 meV per metal atom. Therefore, in the following sections we show the effect of a 75 meV/Fe error on the enthalpies of reaction in our thermodynamic modeling results of Fe^{3+} concentration.

The further details of our DFT method including the endmember supercell setup, equation of state comparison with experiments and the reasons of using HSE06 hybrid functional instead of DFT+U are discussed in the SI section 3.

3. Results

3.1 Integrated model

In general both the oxidation reaction and chg. disp. reaction are possible to occur in either the lower mantle or the experiments. Therefore we first show the integrated model results with both reactions. The model is capable of predicting both $\text{Fe}^{3+}/\Sigma\text{Fe}$ and Fe^0 (metallic Fe) concentrations. The Fe^0 concentration reflects the extent of chg. disp. reaction because the Fe^0 is produced only from this reaction. Fig. 1 shows the $\text{Fe}^{3+}/\Sigma\text{Fe}$ ratio and $2[\text{Fe}^0]/[\text{Fe}^{3+}]$ ratio predicted from the integrated model with respect to $f\text{O}_2$ at $P=100\text{GPa}$, $T=2000\text{K}$. $[\text{Fe}^0]$ and $[\text{Fe}^{3+}]$ denote the number of moles of Fe^0 and Fe^{3+} respectively. $2[\text{Fe}^0]/[\text{Fe}^{3+}]$ shows the extent of chg. disp. reaction: $2[\text{Fe}^0]/[\text{Fe}^{3+}]=1$ means only the chg. disp. reaction occurs in the system while $2[\text{Fe}^0]/[\text{Fe}^{3+}]=0$ indicates all the

Fe^{3+} comes from the oxidation reaction. The relationships between the $f\text{O}_2$ of different capsules are from previous experiments (Pownceby and O'Neil, 1994; Frost et al., 2004).

In Fig.1 there is a transition point of $f\text{O}_2$ ($f\text{O}_2^t$) above which only oxidation reaction occurs and below which only chg. disp. reaction is possible. It is expected that this transition will occur approximately at the $f\text{O}_2$ that can oxidize Fe^0 to Fe^{2+} (where the Fe^{2+} will occur in ferropericlasite), as above that $f\text{O}_2$ no Fe^0 can exist. We don't use any data from FeO or ferropericlasite in constructing our model, so being consistent with Fe^0 /ferropericlasite equilibrium thermodynamics is an important test of the model. In Fig.1 we show the range of the Fe^0 -ferropericlasite equilibrium $f\text{O}_2$ derived from experimental data and an ideal solution model (see SI section 5). The grey region in Fig. 1 is the corresponding $f\text{O}_2$ range from $\text{Fe}\%=5$ to $\text{Fe}\%=40$ in ferropericlasite calculated from ideal solution model. We can see that the transition point occurs at the $f\text{O}_2$ where Fe^0 is in equilibrium with $(\text{Mg}_x\text{Fe}_{1-x})\text{O}$ ($x\approx 0.36$). This result implies that under the $(\text{Mg}_{0.875},\text{Fe}_{0.125})\text{SiO}_3$ compositional condition for Mg-Pv, if we include Fp in the system, the $\text{Fe}\%$ in Fp is about 36 when we have Fe^0 formation and the corresponding equilibrium $f\text{O}_2$ is the $f\text{O}_2^t$ we show in Fig.1. For $f\text{O}_2$ below $f\text{O}_2^t$ the equilibrium will be for lower $\text{Fe}\%$ in Fp, and an $f\text{O}_2$ of about 11.6 corresponds to about $\text{Fe}\%=20$ in the Fp, consistent with values often suggested for the lower mantle (Hirose, 2002). From Fig. 1 we see that our model predicts a range of $f\text{O}_2$ above where Fp with $\text{Fe}\%$ consistent with the lower mantle is stable against forming O_2 gas and Fe^0 and below where O_2 gas starts to be consumed by oxidation of Fe^{2+} to Fe^{3+} in Mg-Pv. This range is therefore where our model (which contains no Al) would predict the $f\text{O}_2$ of the lower mantle to reside, somewhere around 11.6. The ability to define this range consistently for both Mg-Pv and Fp, despite the model being developed without any explicit *ab initio* calculations on the Fp system, supports the accuracy of our thermodynamic model.

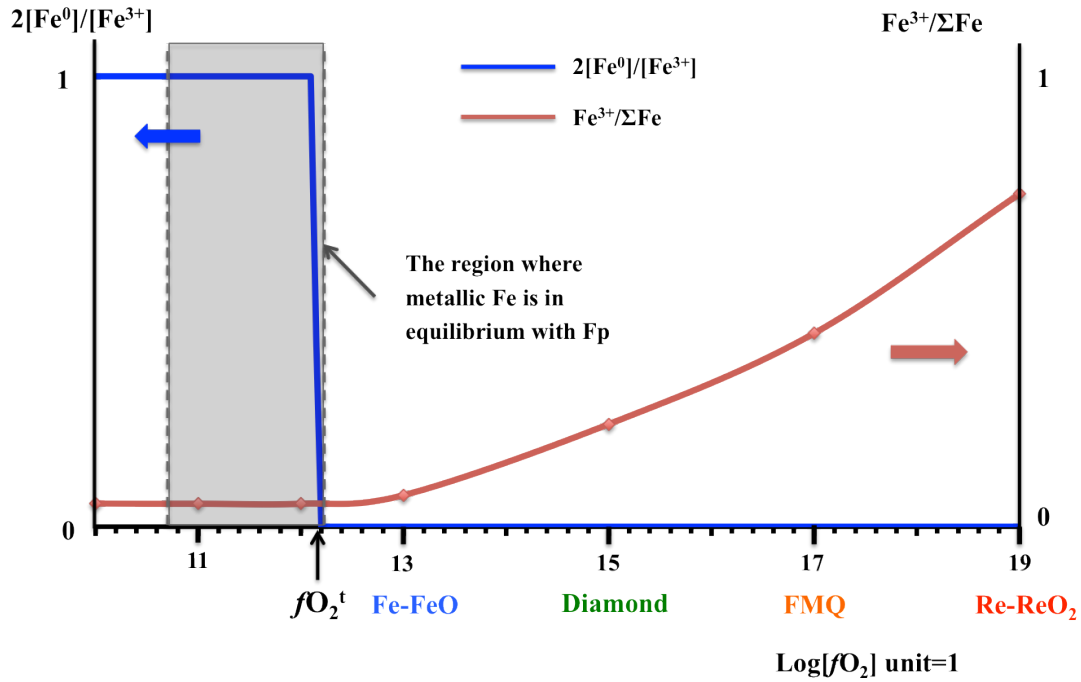


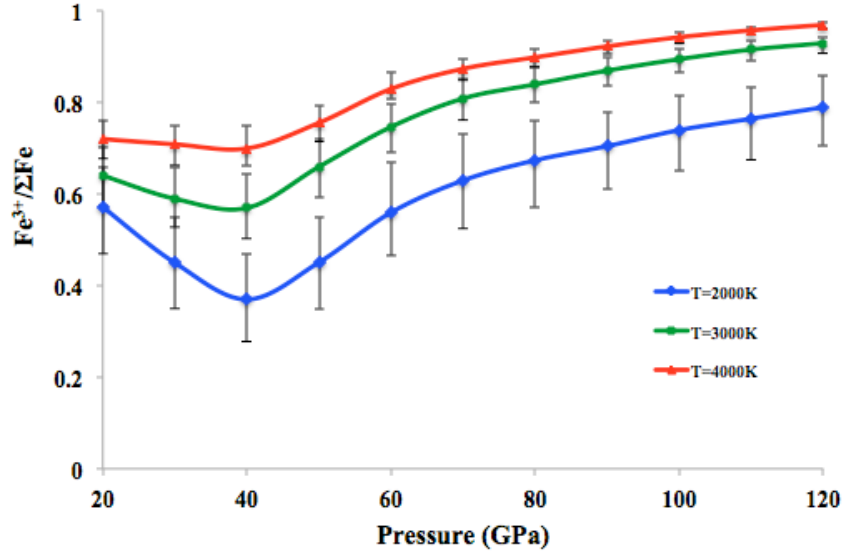
Fig. 1 $2[\text{Fe}^0]/[\text{Fe}^{3+}]$ and $\text{Fe}^{3+}/\Sigma\text{Fe}$ with respect to $f\text{O}_2$ at $T = 2000\text{K}$, $P = 100\text{ GPa}$. The blue curve corresponds to $2[\text{Fe}^0]/[\text{Fe}^{3+}]$ ratio and the red curve corresponds to $\text{Fe}^{3+}/\Sigma\text{Fe}$. The $f\text{O}_2$ of different capsules are from experiments (references in text). The grey region is the Fe^0 -ferropericlasite equilibrium $f\text{O}_2$ at $\text{Fe}\% = 5$ (left boundary) and $\text{Fe}\% = 40$ (right boundary).

In the following sections we apply our thermodynamic model for two different situations. The first situation is to model laboratory experiments. In laboratory experiments the $f\text{O}_2$ is usually buffered by the capsules and has values higher than $f\text{O}_2^t$. As can be seen from Fig. 1, there is no metallic Fe in these higher $f\text{O}_2$ and therefore no chg. disp. reaction. Therefore, we will use our oxidation model to study Fe^{3+} content at different P , T and capsules conditions (see section 3.2). The second situation is to model conditions in the lower mantle. For the lower mantle we assume the stoichiometry consists of a nominally ferrous Mg-Pv and ferropericlasite system (i.e., $(\text{Mg}_{1-x}\text{Fe}_x)\text{SiO}_3 + (\text{Mg}_{1-y}\text{Fe}_y)\text{O}$ and all Fe is Fe^{2+}) from pyrolitic and hartzburgitic compositions, and that this stoichiometry is fixed. We assumed that there is no external free oxygen gas or negligible amount of other oxidizing agents to oxidize Fe^{2+} in the lower mantle. Therefore, in our study, the only possible mechanism to produce Fe^{3+} is the chg. disp. reaction and this reaction will be the

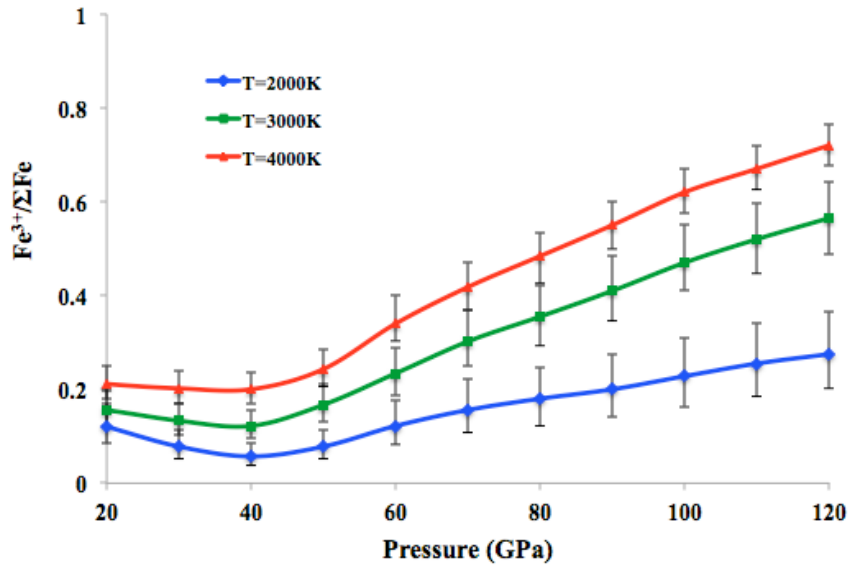
focus of the modeling (see section 3.3). Under these assumptions appropriate for modeling the lower mantle the fO_2 will be below fO_2^t and Fe^0 can be stabilized.

3.2 Oxidation reaction

We calculate the concentration of Fe^{3+} produced by the oxidation reaction from 20 to 120 GPa at 2000, 3000, and 4000 K with fO_2 set by the Re- ReO_2 capsule (higher fO_2) and diamond capsule (lower fO_2) buffers. All the details of capsules and their fO_2 values as a function of pressure are given in the SI section 1. The results of Fe^{3+} concentration in different capsules are shown in **Fig. 2**. In the Al-free system, the oxidation reaction produces a significant amount of Fe^{3+} . The general tendency of $Fe^{3+}/\Sigma Fe$ is that it first decreases up to 40 GPa and then increases. At 2000 K, when the pressure is relatively low, between 20 and 60 GPa, $Fe^{3+}/\Sigma Fe$ is ~ 0.5 in the Re- ReO_2 capsule (higher fO_2) and is about 0.08 in diamond capsule (lower fO_2). When the pressure increases to 100 GPa, $Fe^{3+}/\Sigma Fe$ is ~ 0.7 in Re- ReO_2 and ~ 0.2 in diamond capsule. The ratio is also quite sensitive to temperature and the Fe^{3+} concentration increases when the temperature increases. We also use the model to study the spin transition of Fe^{3+} in the B site of Mg-Pv (**Fig. 3**). Our thermodynamic model indicates a gradual spin transition for the Fe^{3+} in the B site of Mg-Pv. At 2000 K, the spin transition occurs from 30 to 50 GPa. Previous experimental results showed that the spin transition range is 40~60 GPa (Catalli et al., 2010) and simulation results predicted that it is 40~70 GPa (Hsu et al., 2011), which are consistent with this work.



(a)



(b)

Fig. 2 $\text{Fe}^{3+}/\Sigma\text{Fe}$ due to the oxidation reaction (Eq. (1)) at high pressures and temperatures. (a) $\text{Fe}^{3+}/\Sigma\text{Fe}$ in the Re-ReO₂ capsule (higher f_{O_2}) and (b) $\text{Fe}^{3+}/\Sigma\text{Fe}$ in the diamond capsule (lower f_{O_2}). The error bars incorporate the variance of HSE06 hybrid functional result on transition metal oxides, which is taken as ± 75 meV/Fe (Chevrier et al., 2010).

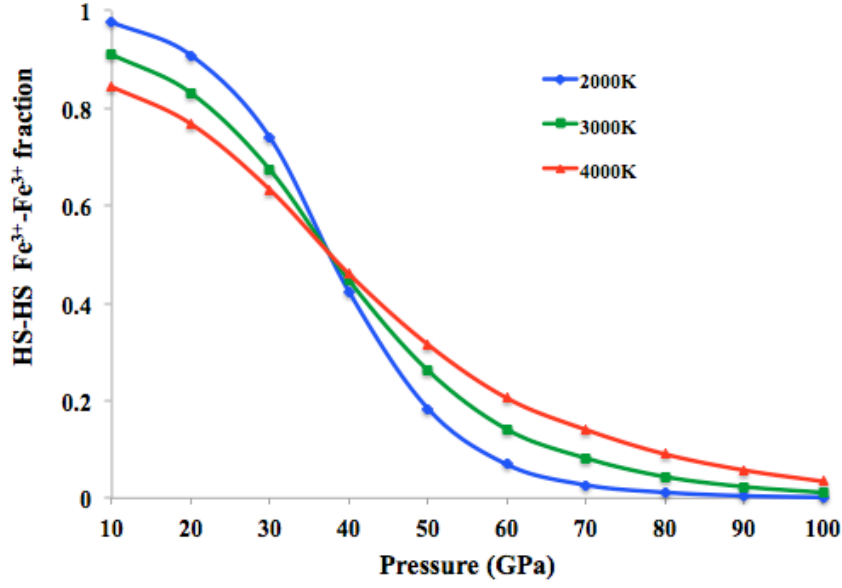
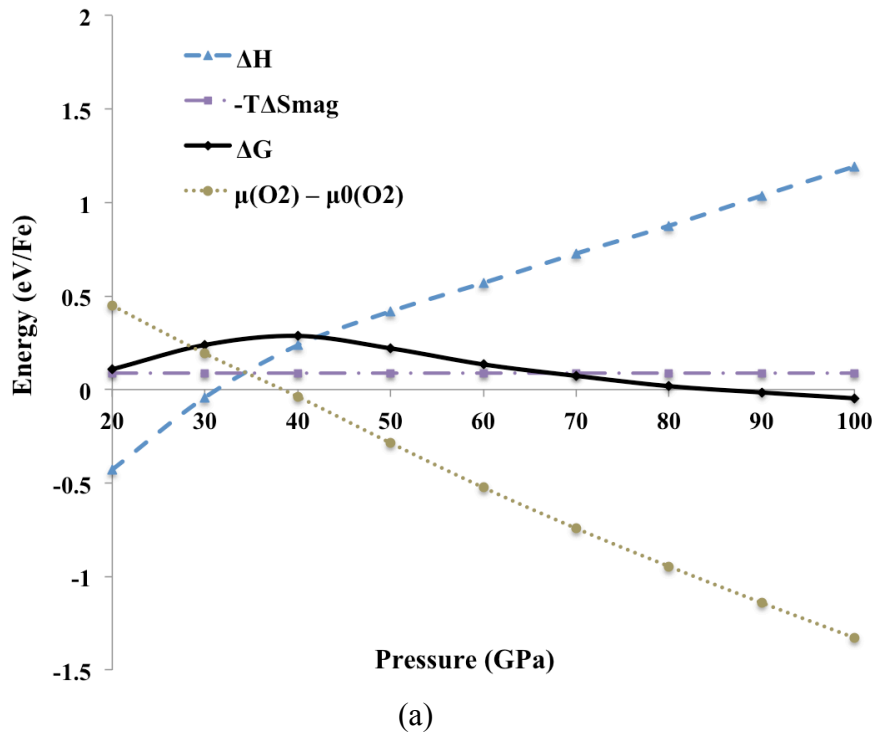


Fig. 3 Spin transition of Fe^{3+} in the B site of ferric Mg-Pv. We show the spin transition with respect to pressures at different temperatures. We denote the fully high-spin state as HS-HS, where the first HS represents the spin state of the Fe^{3+} in the A site and the second HS represents the spin state of the Fe^{3+} in B site in ferric Mg-Pv. The state transforms to HS-LS as the systems undergoes the spin transition.

To better understand what controls the Fe^{3+} concentration, we analyze the energetics of Eq. (4) by separating the Gibbs energy change of the reaction (Eq. (1)) into enthalpy change and entropy change. In the entropy we do not include the configurational entropy as the S_{config} is concentration dependent (it will be discussed later in the next paragraph).

Fig. 4 shows the contribution of each term in ΔG of Eq. (1). In **Fig. 4** (a), ΔG first increases up to 40 GPa and then decreases at higher pressures. The trend in ΔG creates the convex shape of $\text{Fe}^{3+}/\Sigma\text{Fe}$ versus pressure in **Fig. 2**. **Fig. 4** (a) also shows that the concave shape of ΔG is related to the change in slope of ΔH at ~ 40 GPa. In Fig. 4(b), ΔH is further split into $P\Delta V$ and ΔU ($\Delta H = \Delta U + P\Delta V$). It is clear that the $P\Delta V$ also has a slope change at ~ 40 GPa and that the concave shape of $\text{Fe}^{3+}/\Sigma\text{Fe}$ is due to this behavior of the $P\Delta V$ term. This slope change in the $P\Delta V$ term is caused by the spin transition of B site Fe^{3+} from high to low-spin state. Below 40 GPa, the majority spin configuration is the HS-HS ferric Mg-Pv, and $P\Delta V$ increases with pressure going up. We denote the fully high-spin state as HS-HS, where the first HS represents the Fe^{3+} spin state in the A-site

and the second represents Fe^{3+} spin state in B-site in ferric Mg-Pv. When the pressure is ~ 40 GPa, HS-HS ferric Mg-Pv begins to transform into HS-LS Mg-Pv leading to a volume collapse, so the $P\Delta V$ increase rate is reduced significantly around the spin transition pressure. Then, as the pressure increases, all the ferric Mg-Pv is in HS-LS state and the curve is again smooth. So the change in slope is generated in the $P\Delta V$ and also in the ΔH curve. Based on the above analysis, we propose that it is the volume reduction of the spin transition of B site Fe^{3+} that causes the convex shape of the $\text{Fe}^{3+}/\Sigma\text{Fe}$.



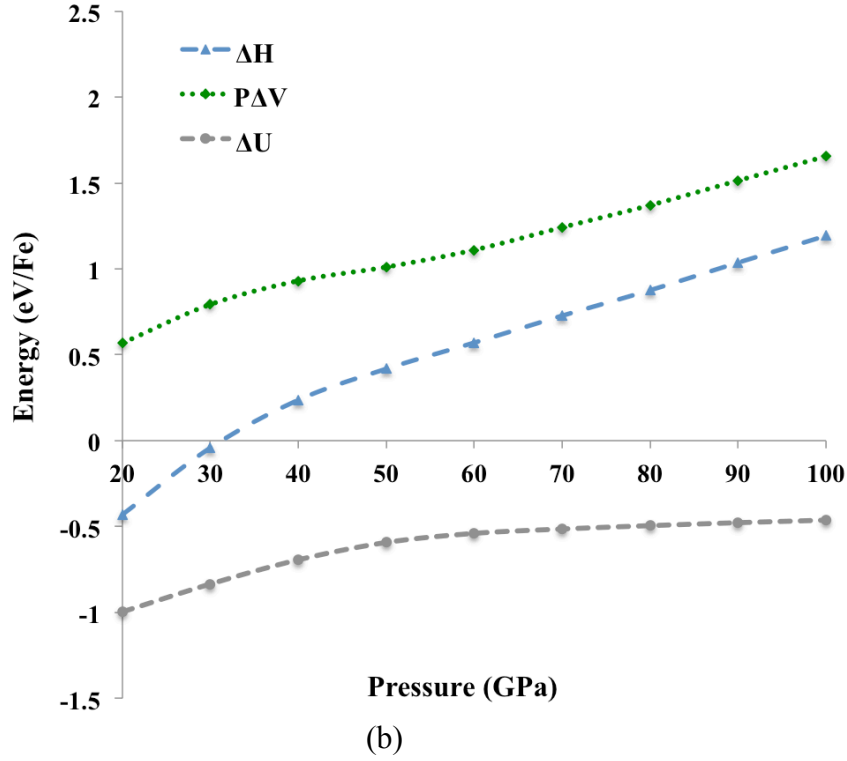


Fig. 4 Changes in thermodynamic quantities with respect to pressure between the right hand side and left hand side of the oxidation reaction in Eq. (1). The lines show change in Gibbs free energy (ΔG), enthalpy (ΔH), internal energy (ΔU), temperature times magnetic entropy ($-T\Delta S_{mag}$), pressure times volume ($P\Delta V$), and the chemical potential difference between O_2 at (T,P) ($\mu(O_2)$) with respect to its reference value at $T = 300$ K, $P = 1$ atm ($\mu_0(O_2)$). Terms are related by $\Delta G = \Delta H - T\Delta S_{mag} = \Delta U + P\Delta V - T\Delta S_{mag}$. All values are shown at $T = 2000$ K for the Re-ReO₂ capsule. The energy is labeled by eV/Fe, which means the system unit we choose has one Fe atom in it. (a) ΔG and its contributions. (b) ΔH and its contributions.

To understand what sets the specific concentration of Fe^{3+} we show in **Fig. 5** the changes in value of each of the terms contributing to $G_{TotalOx}$ (including configurational entropy), as well as the total change in $G_{TotalOx}$ value, as the Fe oxidation occurs. These values are determined from Eq. (4) and take $n = 0$ (pure Fe^{2+}) as the reference (all values are zero for this case). The data are shown as a function of n and for the spin state (γ) which minimizes the total $G_{TotalOx}$ at fixed n , all for 2000 K, 40 GPa, and fO_2 given by Re-ReO₂. We note that n gives the amount of Fe^{3+} , or equivalently, represents the amount of the

reaction in Eq. (1) that has taken place at equilibrium (amount of ferrous Mg-Pv oxidized and transformed to ferric Mg-Pv component). It can be seen clearly that as n increases the enthalpy actually increases, demonstrating that formation of ferric Mg-Pv through the reaction in Eq. (1) is enthalpically unfavorable under these conditions. However, enthalpy increase competes with a decrease in $G_{TotalOx}$ from the configurational entropy contribution, which is the term is $G_{TotalOx}$ primarily driving the formation of Fe^{3+} . The dominant role of configurational entropy explains why $Fe^{3+}/\Sigma Fe$ in Mg-Pv is predicted to be sensitive to temperature.

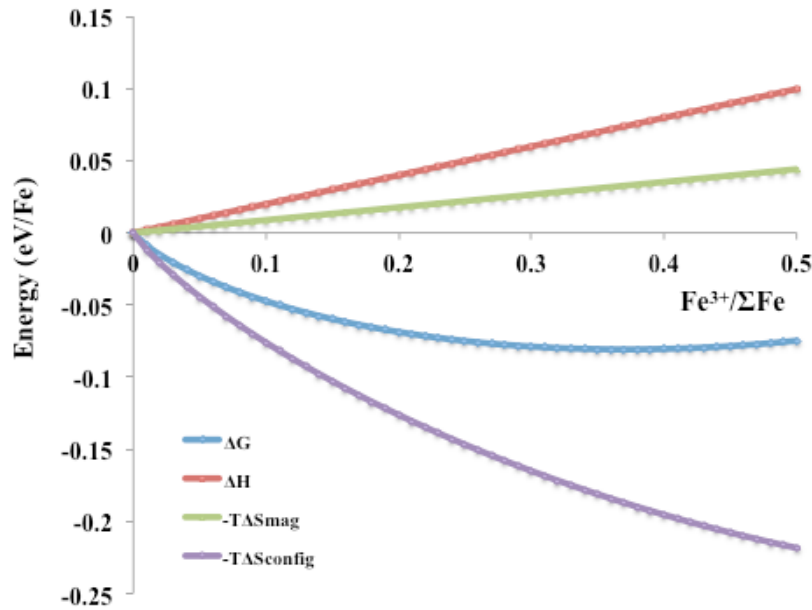


Fig. 5 Changes in total and contributions to the Gibbs free energy as a function of amount of ferrous Fe oxidized to ferric iron ($Fe^{3+}/\Sigma Fe$) under the oxidation reaction. Note that the variable n from Eq. (4) is equal to the $Fe^{3+}/\Sigma Fe$ ratio in this figure. $\Delta G(Fe^{3+}/\Sigma Fe) = \Delta H(Fe^{3+}/\Sigma Fe) - T\Delta S_{mag}(Fe^{3+}/\Sigma Fe) - T\Delta S_{config}(Fe^{3+}/\Sigma Fe)$. Terms are taken from Eq. (4) and evaluated at $T = 2000$ K, $P = 40$ GPa, and f_{O_2} given by Re-ReO₂. The results show that the increase in configurational entropy drives the Fe oxidation.

3.3 Charge disproportionation

In this section we calculate the Fe^{3+} produced by the chg. disp. reaction in Eq. (9) from 20 to 120 GPa at 2000, 3000, and 4000 K. This mechanism was proposed by some previous studies to be a major source of valence state change of Fe under the lower

mantle conditions (Frost et al., 2004; Lauterbach et al., 2000; Zhang and Oganov, 2006), where the fO_2 is expected to be very low. The chg. disp. reaction also produces metallic Fe in the lower mantle (Frost et al., 2004). Previous simulation (Zhang and Oganov, 2006) predicted chg. disp. reaction in both Al-free and Al-bearing system and experimental (Frost et al., 2004; Lauterbach et al., 2000; Grocholski et al., 2009) studies suggested Fe disproportionation in Al-bearing systems. But there were some significant discrepancies between experiments and simulation. In particular, previous calculations of the enthalpy change of the chg. disp. reaction (Eq. (9)) for both Al-bearing and Al-free cases predicted a negative value of -1.13 eV/Fe and -1.03 eV/Fe respectively, suggesting that the chg. disp. reaction goes to near completion and almost all Fe^{2+} will be transformed to Fe^{3+} (i.e., $Fe^{3+}/\Sigma Fe \approx 1$). However, the values of $Fe^{3+}/\Sigma Fe$ in experiments are at most about 0.2~0.3 for Al-free Mg-Pv and 0.6 for Al-bearing Mg-Pv. The discrepancy suggests that there is significant uncertainty about the driving forces and extent of the chg. disp. reaction in Mg-Pv.

In this work, the predicted Fe^{3+} content by chg. disp. reaction is shown in **Fig. 6**. We emphasize that these predictions are independent of fO_2 provided fO_2 is less than fO_2^\dagger in Fig. 1. The extent of chg. disp. reaction is much lower than that predicted from the oxidation reaction. From 20 to 120 GPa, the Fe^{3+} fraction is only around 0.01~0.07 at 2000 K. Even at 4000 K, which is likely higher than the temperature for most of the lower mantle, the Fe^{3+} concentration from chg. disp. reaction is still quite limited, predicted to be about 0.08~0.15. Similarly to the oxidation reaction, we predict that the enthalpy of the chg. disp. reaction is positive and that the Fe^{3+} formation is driven by gains in configurational entropy, which implies that $Fe^{3+}/\Sigma Fe$ is sensitive to temperature.

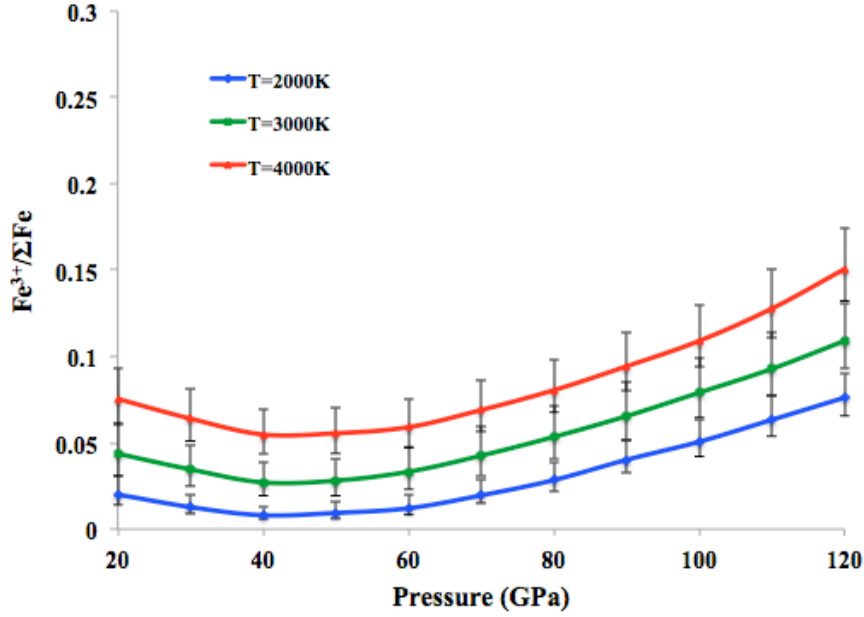


Fig. 6 $\text{Fe}^{3+}/\Sigma\text{Fe}$ due to the chg. disp. reaction only at different pressures and temperatures. The error bar incorporates the variance of HSE06 hybrid functional result on transition metal oxides, which is taken as ± 75 meV/Fe (Chevrier et al., 2010).

Similar to the results in the oxidation reaction, the Fe^{3+} concentration first decreases and then increases with pressure. As with the oxidation reaction, the turning point is at ~ 40 GPa and can be explained by the B-site spin transition. **Fig. 7** shows the energetics of Eq. (9) by splitting the Gibbs energy change into $\Delta H (= \Delta U + P\Delta V)$ and $-T\Delta S_{mag}$. The result is similar to **Fig. 4** in that a change in slope in the $P\Delta V$ curve leads to a convex shape of ΔH and ΔG . Before the spin transition, the reaction in of Eq. (9) causes a volume increase, after the spin transition it leads to a volume decrease, where the change is due to smaller size of LS with respect to HS Fe^{3+} in the final state. As ΔV changes from positive to negative the value of $P\Delta V$ changes sign as well. The shift in sign of this term changes ΔH from increasing to decreasing with pressure, which then leads to the convex shape of $\text{Fe}^{3+}/\Sigma\text{Fe}$ as a function of pressure.

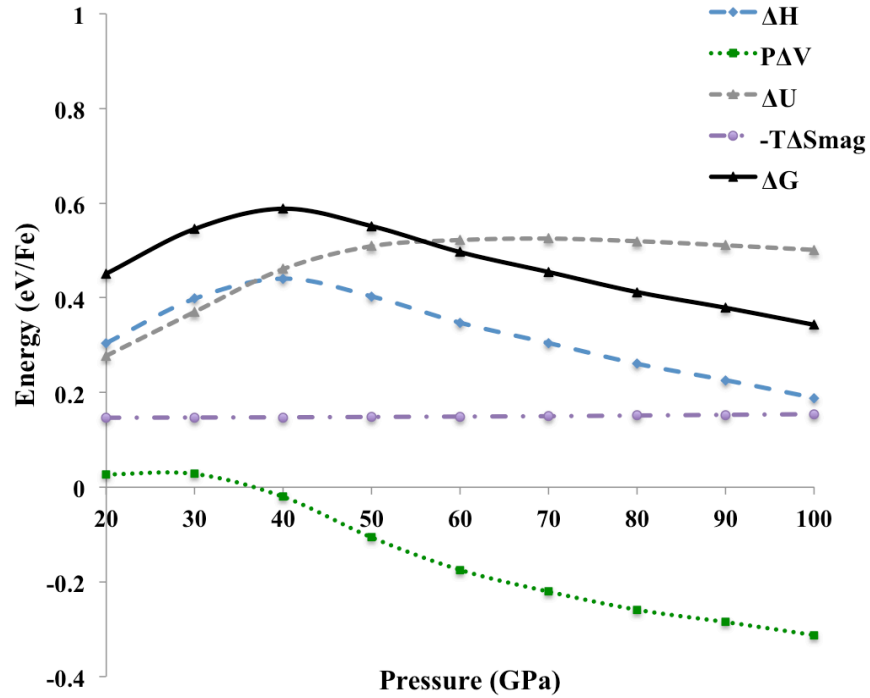


Fig. 7 Changes in thermodynamic quantities with respect to pressure between the right- and left-hand sides of the chg. disp. reaction in Eq. (9). The lines show change in Gibbs free energy (ΔG), enthalpy (ΔH), internal energy (ΔU), temperature times magnetic entropy ($-T\Delta S_{mag}$), and pressure times volume ($P\Delta V$). Terms are related by $\Delta G = \Delta H - T\Delta S_{mag} = \Delta U + P\Delta V - T\Delta S_{mag}$. All values are shown at $T = 2000$ K. The energy is labeled by eV/Fe, which means the system unit we choose has one Fe atom in it.

We also calculate the Al-free $\text{Fe}^{3+}/\Sigma\text{Fe}$ contribution from chg. disp. reaction under specifically lower mantle conditions, as shown in in **Fig. 8**. We set the lower mantle T - P by using the geotherm by Brown and Shankland (1981).

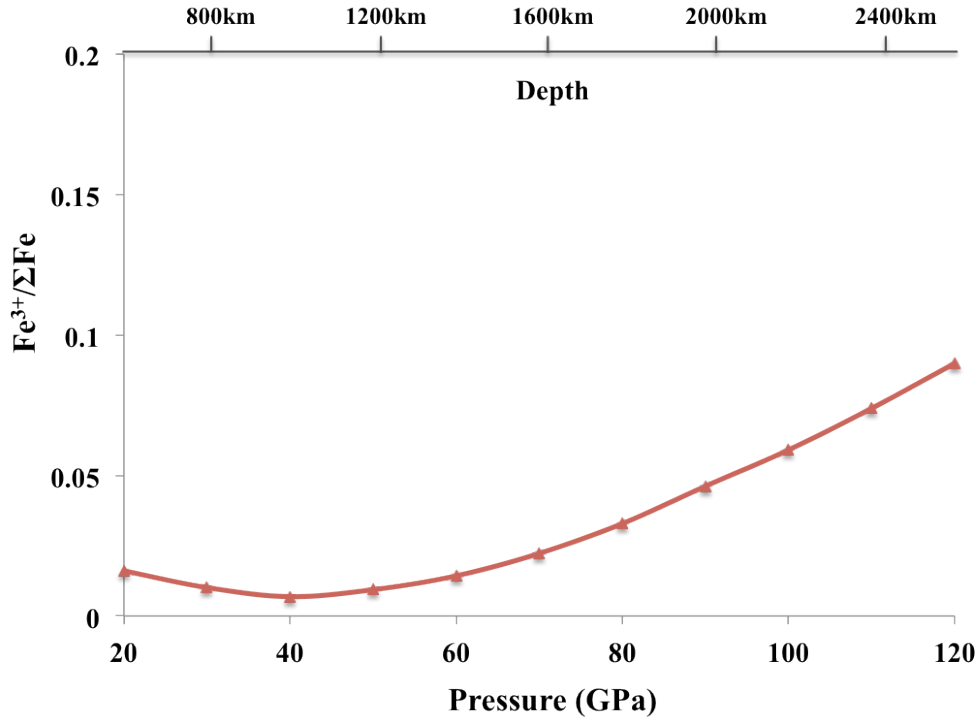


Fig. 8 Calculated $\text{Fe}^{3+}/\Sigma\text{Fe}$ in Mg-Pv with respect to pressures from chg. disp. reaction under lower mantle geotherm (Brown and Shankland (1981)) P - T condition.

4. Discussion

4.1 Validation of the model

Experimental studies have shown that $\text{Fe}^{3+}/\Sigma\text{Fe}$ is about 0.2~0.3 in the Re-ReO₂ capsule and close to zero in the diamond capsule in Al-free Mg-Pv at 25~30 GPa and 2000 K (Lautherbach et al., 2000; Frost et al., 2002). In our modeling result, $\text{Fe}^{3+}/\Sigma\text{Fe}$ is about 0.4-0.5 in the Re-ReO₂ capsule and 0.08-0.1 in the diamond capsule at the same P - T range.

Our modeling results are slightly higher than the experimental results for $\text{Fe}^{3+}/\Sigma\text{Fe}$. One source of this discrepancy may be kinetic limitations in the experiments. Whereas our modeling work is based on the thermodynamic equilibrium (minimization of the total Gibbs energy), in experiments there may be kinetic effects limiting the formation of Fe^{3+} . We predict that the dominant mechanism for forming Fe^{3+} in many experiments is the oxidation reaction of Fe^{2+} in the A-site of Mg-Pv to Fe^{3+} in both A- and B-sites in Al-free Mg-Pv. This reaction requires diffusion of some Fe ions from A to B sites. The kinetic

barrier for the Fe^{3+} diffusion between different sites and the associated Mg vacancy migration could prevent some Fe^{2+} being oxidized to Fe^{3+} , which would decrease $\text{Fe}^{3+}/\Sigma\text{Fe}$. According to the two reactions we consider in this work Eq. (1) and Eq. (9), when Fe^{3+} enters the Mg-Pv by charge coupled substitution, diffusion of a Mg vacancy must also occur. According to Ammann et al. (2010), the kinetic barriers for Mg vacancy mediated migration at 30 GPa is about 4.0 eV. The diffusion coefficient can be

$$D = a^2 \nu \times \exp\left(-\frac{E_{\text{barrier}}}{kT}\right),$$

approximately estimated from this barrier using the relationship:

where a is the hop length and ν is the attempt frequency. Taking reasonable values of $a = 3\text{\AA}$ which is about the Mg-Mg distance in Mg-Pv and $\nu = 5 \times 10^{12}$ Hz we can estimate D and thereby assess kinetic effects. We assume that the associated transport of Mg vacancy requires diffusion of relevant species at least to the grain boundary between MgO and Mg-Pv. This assumption is supported by the observation that when we have a Mg vacancy created in the system, the vacancy has to diffuse to the MgO/Mg-Pv boundary to react with MgO and compensate the vacancy, as shown in **Eq. (1)** and **Eq. (9)**. From the TEM images of Mg-Pv coexisting with MgO (Frost et al., 2004; Irifune et al., 2010), the length scale of the Mg-Pv grain is about $5\ \mu\text{m}$, so the total diffusion length for Mg vacancies migrating to the grain boundary is about $L = 2.5\ \mu\text{m}$. The diffusion time is approximately given by $t = L^2/6D$. Therefore at 30 GPa and 2000 K, the total diffusion time for Mg vacancies to the grain boundary is about 8 hrs. However, in some relevant experiments to date the Mg-Pv sample was under high P - T for less than 8 hrs, for example: 2 hrs (Sinmyo et al., 2008), 2 hrs (Lauterbach et al., 2000). Although the estimates for diffusion times and associated time to produce Fe^{3+} are very approximate, this analysis suggests that the experimental duration may not be sufficiently long to allow the system to evolve into complete thermal equilibrium. Furthermore, the rate of the oxidation reaction will slow down as more Fe^{3+} forms and the configurational entropy driving force becomes weaker. From Fig. 5 it is clear that the gain in Gibbs energy from forming additional Fe^{3+} becomes very minor as the concentration approaches its equilibrium value.

Another likely source for discrepancies between the model and the experiment is uncertainties in the ab initio energetics and/or equations of state. To obtain values closer to experiment, e.g., $\text{Fe}^{3+}/\Sigma\text{Fe} = 0.25$ in the Re-ReO₂ capsule and 0.05 in the diamond capsule at 2000 K and 30 GPa, our reaction energies would have to be increased by about 0.17 eV/Fe and 0.10 eV/Fe, which correspond to a change in reaction volume of 0.89 Å³/Fe and 0.52 Å³/Fe, respectively. While these energy errors are larger than the 75 meV/Fe we used in our estimated error bars, they are not outside the range of errors sometimes seen in transition metal oxide calculations (Chevrier et al., 2010).

Overall, it is possible that both errors in model energetics and some kinetic limitations in the experiments lead to the observed discrepancies. However, the level of agreement for $\text{Fe}^{3+}/\Sigma\text{Fe}$, especially in light of the excellent agreement between the calculated and measured equation of state parameters (see Table S4), suggests that the model is robust enough to make useful prediction for mechanisms, trends, and perhaps even quantitative values for the Fe^{3+} formation.

Zhang and Oganov (2006) performed a pioneering series of ab-initio reaction enthalpy calculations for the chg. disp. reaction given in Eq. (9) and found a large negative ΔH , suggesting nearly complete chg. disp. However, our thermodynamic modeling indicates that the configurational entropy drives the reactions and the ΔH is positive (Figs 4, 5, 7). This difference comes from the fact that Zhang and Oganov (2006) used standard GGA to calculate the enthalpy difference of the chg. disp. reaction. Their paper was the first DFT simulation work to provide us with insights about the formation energetics of Fe^{3+} from Fe^{2+} , but they faced many challenges in accurately treating transition metal oxide energetics. In particular, techniques for treating correlated electron systems with the HSE06 hybrid functional hadn't been well studied and the various U values for Fe in Mg-Pv were not yet known then. Based on the previous discussion about the accuracy of HSE06 functional and the work of Chevrier et al., (2010), we believe that our HSE06 hybrid functional calculations are significantly more reliable than the previous standard GGA studies of Zhang and Oganov (2006).

Diamond-anvil cell studies have suggested similar level of $\text{Fe}^{3+}/\Sigma\text{Fe}$ in Mg-Pv as that reported in multi-anvil press studies at greater depth conditions. Whereas multi-anvil press experiments controlled $f\text{O}_2$ of the samples through various methods (Frost et al., 2004; Lautherbach et al., 2000), the exact $f\text{O}_2$ was unknown in almost all the diamond-anvil cell experiments, except for Grocholski et al (2009, GRL) where metallic iron powder was added in an attempt to regulate $f\text{O}_2$ to reducing conditions. Our study uses the $f\text{O}_2$ of the capsule materials to approximate the $f\text{O}_2$ in the sample chamber and suggests that $\text{Fe}^{3+}/\Sigma\text{Fe}$ can be highly sensitive to $f\text{O}_2$ at least in Al-free Mg-Pv and therefore it is important to make attempts to control and measure $f\text{O}_2$ in diamond-anvil cell synthesis of Mg-Pv.

4.2 Geophysical implications of the modeling

Our thermodynamic model in this work only focuses on the Al-free Mg-Pv and therefore can be used to model lower-mantle regions with low Al content. In pyrolite, which is believed to be average composition of the mantle, at 20~25 GPa, Irifune et al. (2010) showed that most Al remains in majoritic garnet and Mg-Pv contains little Al. Therefore, our model predicts that in the uppermost lower mantle, where Al content is low in Mg-Pv, the formation of Fe^{3+} is unfavorable and therefore the Fe^{3+} concentration in Mg-Pv and the content of metallic Fe are expected to be very low. We predict that the upper bound of equilibrium $\text{Fe}^{3+}/\Sigma\text{Fe}$ in Mg-Pv is about 0.015 at 25 GPa at mantle temperature, as indicated from **Fig. 8**.

Harzburgite, a depleted mantle composition, is expected to exist in the mantle, including the lower mantle, through subduction of oceanic lithosphere. It contains much smaller amount of Al than pyrolite and therefore Mg-Pv in this composition may contain substantially lower Al (Xu et al., 2008). Our results suggest such heterogeneities will contain Mg-Pv with very little Fe^{3+} and metallic iron.

One of the most intriguing observations for geophysics in our study is that $\text{Fe}^{3+}/\Sigma\text{Fe}$ in Mg-Pv may not stay constant with depth in the lower mantle. Within our model this is not due to changes in oxygen content but changes in the extent of the chg. disp. reaction.

In some recent geochemical models, $\text{Fe}^{3+}/\Sigma\text{Fe}$ in Mg-Pv has been a central property in explaining metal-silicate partitioning during core formation and elevation of upper-mantle $f\text{O}_2$ to current level (Wood et al., 2006; Frost and McCammon, 2008; McCammon, 2005). However, in these models, $\text{Fe}^{3+}/\Sigma\text{Fe}$ in Mg-Pv is assumed to be constant at different depths in the lower mantle. Our study reveals that effects from spin transition and temperature can result in complex radial variations in $\text{Fe}^{3+}/\Sigma\text{Fe}$ (at least in Al-free Mg-Pv) due to changes in the extent of the chg. disp. reaction, even if the oxygen content of the lower mantle remains constant. Although the magnitude is small, our study suggests that the mid mantle may contain less Fe^{3+} in Mg-Pv than the rest of the mantle. The lowermost mantle is a thermal boundary layer and temperature is expected to increase rapidly with depth from ~ 2500 K to ~ 4500 K within 200-400 km depth interval. Whereas Mg-Pv may transform to the post-perovskite phase in the lowermost mantle, warm regions in the lowermost mantle will be still dominated by Mg-Pv due to the strong positive Clapeyron slope of the post-perovskite boundary (Shim, 2008; Tateno, 2009). Large Low Shear Velocity Provinces (LLSVPs) have been identified in the lowermost mantle (Garnero and McNamara, 2008). The low velocities of the regions are often attributed to enrichment in Fe and elevated temperature in the heterogeneity (McNamara, 2005). Our models predict that Fe^{3+} concentration in Mg-Pv may reach the maximum due to the possible thermal effects in LLSVP. The elevation of the Fe^{3+} concentration may alter the physical properties of Mg-Pv, possibly affecting seismic properties (such as density and bulk modulus) and transport properties (such as thermal and electrical conductivities) (Catalli et al., 2011; Goncharov et al., 2008), and therefore may have impact on the dynamic stability of LLSVPs in the lowermost mantle.

5. Conclusion

We use an ab-initio based thermodynamic model to study the origin and extent of Fe^{3+} formation in Al-free Mg-Pv. The model uses the accurate HSE06 functional to treat the correlation effects associated with the Fe and finds good agreement with the equation of state and the spin transition pressure of Fe^{3+} in the B site of ferric Mg-Pv reported in

previous models and experiments. We consider two mechanisms for the Fe^{3+} formation: (a) the oxidation reaction and (b) the charge disproportionation reaction. For both reactions this work suggests that, contrary to previous models, the configurational entropy is the driving force to form Fe^{3+} and that Fe^{3+} is not favored by enthalpy gains under lower-mantle or typical experimental conditions. This dominance of entropy results in a strong temperature dependence of $\text{Fe}^{3+}/\Sigma\text{Fe}$. The oxidation reaction is the dominant mechanism producing Fe^{3+} in laboratory experiments with buffering from capsules that control the $f\text{O}_2$ at a relative high level compared to the Fe – ferropericlasite equilibrium. Simulated $\text{Fe}^{3+}/\Sigma\text{Fe}$ in the Re-ReO₂ and diamond capsules is qualitatively consistent with the experiments and discrepancies may be in part due to only partial equilibration during the experiments. The model predicts that the charge disproportionation reaction will yield an $\text{Fe}^{3+}/\Sigma\text{Fe}$ ratio of about 0.01~0.07 at lower-mantle conditions in Al-free Mg-Pv. This result suggests Fe^{3+} concentration is very limited in the absence of dissolved Al in the Mg-Pv. Thus we expect limited Fe^{3+} for Mg-Pv in the uppermost region of the lower mantle (25~30 GPa) and Mg-Pv in harzburgite throughout the lower mantle, as both contain very little Al. Our results also suggest that $\text{Fe}^{3+}/\Sigma\text{Fe}$ in Al-free Mg-Pv does not remain constant in the lower mantle but may be low in the mid mantle and reach a maximum at the core-mantle boundary region.

Acknowledgement

Morgan and Shim gratefully acknowledge support from the National Science Foundation (NSF) for this work (NSF-EAR1316022). Computing resources in this work benefitted from the use of the Extreme Science and Engineering Discovery Environment (XSEDE), which is supported by National Science Foundation grant number OCI-1053575.

References:

- Ammann, M.W., Brodholt, J.P., Wookey, J., Dobson, D.P., 2010. First-principles constraints on diffusion in lower-mantle minerals and a weak D' layer. *Nature* 465, 462–5.
- Anisimov, V.I., Zaanen, J., Andersen, O.K., 1991. Band theory and Mott insulators: Hubbard U instead of Stoner I. *Physical Review B* 44, 943–954.
- Auzende, A.-L., Badro, J., Ryerson, F.J., Weber, P.K., Fallon, S.J., Addad, A., Siebert, J., Fiquet, Guillaume, 2008. Element partitioning between magnesium silicate perovskite and ferropericlasite: New insights into bulk lower-mantle geochemistry. *Earth and Planetary Science Letters* 269, 164–174.
- Ashcroft, N.W., Mermin, N.D., 1976. *Solid State Physics*, Appendix C, 760-761.
- Badro, J., Fiquet, Guillaume, Guyot, F., Rueff, J.-P., Struzhkin, V. V, Vankó, G., Monaco, G., 2003. Iron partitioning in Earth's mantle: toward a deep lower mantle discontinuity. *Science (New York, N.Y.)* 300, 789–91.
- Bengtson, A., Persson, K., Morgan, D., 2008. Ab initio study of the composition dependence of the pressure-induced spin crossover in perovskite ($\text{Mg}_{1-x}\text{Fe}_x$) SiO_3 . *Earth and Planetary Science Letters* 265, 535–545.
- Bloch, P.E., 1994. Projector Augmented-wave Method. *Physical Review B* 50, 17953–17979.
- Bovolo, C.I., 2005. The physical and chemical composition of the lower mantle. *Philosophical transactions. Series A, Mathematical, physical, and engineering sciences* 363, 2811–2836.
- Brodholt, J.P., 2000. Pressure-induced changes in the compression mechanism of aluminous perovskite in the Earth's mantle. *Nature* 407, 620-622.
- Brown, J.M., Shankland, T.J., 1981. Thermodynamic parameters in the Earth as determined from seismic profiles. *Geophys. J.R. astr. Soc.* 66, 579–596.
- Campbell, A.J., Danielson, L., Righter, K., Seagle, C.T., Wang, Y., Prakapenka, Vitali B., 2007. Pressure-Volume-Temperature study of metal-oxide pairs. Poster presented in 2007 COMPRESS Annual Meeting, Fairlee, Vermont.
- Campbell, A.J., Danielson, L., Righter, K., Seagle, C.T., Wang, Y., Prakapenka, Vitali B., 2009. High pressure effects on the iron–iron oxide and nickel–nickel oxide oxygen fugacity buffers. *Earth and Planetary Science Letters* 286, 556–564.

- Catalli, K., Shim, S.H., Dera, P., Prakapenka, V. B., Zhao, J., Sturhahn, W., Chow, P., Xiao, Y., Cynn, H., Evans, W.J., 2011. Effects of the Fe³⁺ spin transition on the properties of aluminous perovskite—New insights for lower-mantle seismic heterogeneities. *Earth and Planetary Science Letters* 310, 293–302.
- Catalli, K., Shim, S.H., Prakapenka, V. B., Zhao, J., Sturhahn, W., Chow, P., Xiao, Y., Liu, H., Cynn, H., Evans, W., 2010. Spin state of ferric iron in MgSiO₃ perovskite and its effect on elastic properties. *Earth and Planetary Science Letters* 289, 68–75.
- Chevrier, V.L., Ong, S.P., Armiento, R., Chan, M.K.Y., Ceder, G., 2010. Hybrid density functional calculations of redox potentials and formation energies of transition metal compounds. *Physical Review B* 82, 075122.
- Dubrovinsky, L., Saxena, S., Tutti, F., Rekhi, S., LeBehan, T., 2000. In situ X-Ray study of thermal expansion and phase transition of iron at multimegabar pressure. *Physical review letters* 84, 1720–3.
- Fiquet, G., Dewaele, A., Andrault, D., Kunz, M., Bihan, T.L., 2000. Thermoelastic properties and crystal structure of MgSiO₃ perovskite at lower mantle pressure and temperature conditions. *Geophysical Research Letters* 27, 21–24.
- Frost, D.J., Langenhorst, F., 2002. The effect of Al₂O₃ on Fe-Mg partitioning between magnesiowustite and magnesium silicate perovskite. *Earth and Planetary Science Letters* 199, 227–241.
- Frost, D.J., Liebske, C., Langenhorst, F., 2004. Experimental evidence for the existence of iron-rich metal in the Earth's lower mantle. *Nature* 409–412.
- Frost, D.J., McCammon, C.A., 2008. The redox state of Earth's mantle. *Annual Review of Earth and Planetary Sciences* 36, 389-420.
- Garnero, E.J., McNamara, A.K., 2008. Structure and dynamics of Earth's lower mantle. *Science* 320, 626-628.
- Goncharov, A.F., Haugen, B.D., Struzkin, V.V., Beck, P., Jacobsen, S.D., 2008. Radiative conductivity in the Earth's lower mantle. *Nature* 456, 231-234.
- Grocholski, B., Shim, S.H., Sturhahn, W., Zhao, J., Xiao, Y., Chow, P.C., 2009. Spin and valence states of iron in (Mg_{0.8}Fe_{0.2})SiO₃ perovskite. *Geophysical Research Letters* 36, L24303.
- Heyd, J., Scuseria, G.E., Ernzerhof, M., 2003. Hybrid functionals based on a screened Coulomb potential. *The Journal of Chemical Physics* 118, 8207.

- Heyd, J., Scuseria, G.E., Ernzerhof, M., 2006. Erratum: “Hybrid functionals based on a screened Coulomb potential” [J. Chem. Phys. 118, 8207 (2003)]. The Journal of Chemical Physics 124, 219906.
- Hirose, K., 2002. Phase transitions in pyrolitic mantle around 670-km depth: implications for upwelling of plumes from the lower mantle. Journal of Geophysical Research 107, 2078.
- Hsu, H., Blaha, P., Cococcioni, M., Wentzcovitch, R., 2011. Spin-State Crossover and Hyperfine Interactions of Ferric Iron in MgSiO_3 Perovskite. Physical Review Letters 106, 1–4.
- Hsu, H., Umemoto, K., Blaha, P., Wentzcovitch, Renata M., 2010. Spin states and hyperfine interactions of iron in $(\text{Mg,Fe})\text{SiO}_3$ perovskite under pressure. Earth and Planetary Science Letters 294, 19–26.
- Hsu, H., Yu, Y.G., Wentzcovitch, Renata M., 2012. Spin crossover of iron in aluminous MgSiO_3 perovskite and post-perovskite. Earth and Planetary Science Letters 359–360, 34–39.
- Irifune, T., Shinmei, T., McCammon, C. a, Miyajima, N., Rubie, D.C., Frost, Daniel J, 2010. Iron partitioning and density changes of pyrolite in Earth’s lower mantle. Science (New York, N.Y.) 327, 193–5.
- Jackson, J.M., 2005. A synchrotron Mossbauer spectroscopy study of $(\text{Mg,Fe})\text{SiO}_3$ perovskite up to 120 GPa. American Mineralogist 90, 199–205.
- Jacobsen, S.D., Reichmann, H., Spetzler, H.A., Mackwell, S.J., Smyth, J.R., Angel, R.J., Mccammon, C.A., 2002. Structure and elasticity of single-crystal $(\text{Mg,Fe})\text{O}$ and a new method of generating shear waves for gigahertz ultrasonic interferometry. Journal of Geophysical Research 107, 2037.
- Karato, S., 2003. The Dynamic Structure of the Deep Earth – An Interdisciplinary Approach
- Kesson, S.E., Fitz Gerald, J.D., Shelley, J.M., 1998. Mineralogy and dynamcis of a pyrolite lower mantle. Nature 393, 3–6.
- Lauterbach, S., McCammon, C., Van Aken, P., Langenhorst, F., Seifert, F., 2000. Mossbauer and ELNES spectroscopy of $(\text{Mg,Fe})(\text{Si,Al})\text{O}_3$ perovskite: a highly oxidised component of the lower mantle. Contrib Mineral Petrol 138, 17–26.
- Lee, Y.-L., Morgan, D., 2012. Ab initio and empirical defect modeling of $\text{LaMnO}_{(3\pm\delta)}$ for solid oxide fuel cell cathodes. Physical chemistry chemical physics : PCCP 14, 290–302.

- Lin, J., Alp, E., Mao, Z., 2012. Electronic spin states of ferric and ferrous iron in the lower-mantle silicate perovskite. *American Mineralogist* 97, 592–597.
- Lin, J.-F., Struzhkin, V. V., Jacobsen, S.D., Hu, M.Y., Chow, Paul, Kung, J., Liu, Haozhe, Mao, H.-K., Hemley, Russell J., 2005. Spin transition of iron in magnesiowüstite in the Earth's lower mantle. *Nature* 436, 377–80.
- Lundin, S., Catalli, K., Santillán, J., Shim, S.-H., Prakapenka, V.B., Kunz, M., Meng, Y., 2008. Effect of Fe on the equation of state of mantle silicate perovskite over 1Mbar. *Physics of the Earth and Planetary Interiors* 168, 97–102.
- Mao, H., 1997. Multivariable Dependence of Fe-Mg Partitioning in the Lower Mantle. *Science* 278, 2098–2100.
- Mao, Z., Lin, J.F., Liu, J., Prakapenka, V. B., 2011a. Thermal equation of state of lower-mantle ferropericlase across the spin crossover. *Geophysical Research Letters* 38, L23308.
- Mao, Z., Lin, J.F., Scott, H.P., Watson, H.C., Prakapenka, V.B., Xiao, Y., Chow, P., McCammon, C., 2011b. Iron-rich perovskite in the Earth's lower mantle. *Earth and Planetary Science Letters* 309, 179–184.
- Mathon, O., Baudalet, F., Itié, J., Polian, a., d'Astuto, M., Chervin, J., Pascarelli, S., 2004. Dynamics of the Magnetic and Structural α - ϵ Phase Transition in Iron. *Physical Review Letters* 93, 255503.
- McCammon, C., 1997. Perovskite as a possible sink for ferric iron in the lower mantle. *Nature* 387, 694–696.
- McCammon, C., 1998. The crystal chemistry of ferric iron in $\text{Fe}_{0.05}\text{Mg}_{0.95}\text{SiO}_3$ perovskite as determined by Mossbauer spectroscopy in the temperature range 80-293K. *Physics and Chemistry of Minerals* 25, 292-300.
- McCammon, C., 2005. The Paradox of Mantle Redox. *Science* 308, 807–808.
- McCammon, C., Lauterbach, S., Seifert, F., Langenhorst, F., Van Aken, P., 2004. Iron oxidation state in lower mantle mineral assemblages. *Earth and Planetary Science Letters* 222, 435–449.
- McNamara, A.K., Zhong, S., 2005. Thermochemical Structures Beneath Africa and the Pacific Ocean, *Nature* , 437, 1136-1139.
- Metsue, A., Tsuchiya, T., 2012. Thermodynamic properties of $(\text{Mg},\text{Fe}^{2+})\text{SiO}_3$ perovskite at the lower-mantle pressures and temperatures: an internally consistent LSDA+U study. *Geophysical Journal International* 190, 310–322.

- Murakami, M., Hirose, K., Kawamura, K., Sata, N., Ohishi, Y., 2004. Post-Perovskite Phase Transition in MgSiO_3 . *Science* (New York, N.Y.) 304, 855–858.
- Nakajima, Y., Frost, Daniel J., Rubie, D.C., 2012. Ferrous iron partitioning between magnesium silicate perovskite and ferropericlase and the composition of perovskite in the Earth's lower mantle. *Journal of Geophysical Research* 117, B08201.
- Paier, J., Marsman, M., Hummer, K., Kresse, G., Gerber, I.C., Ángyán, J.G., 2006. Erratum: "Screened hybrid density functionals applied to solids" [*J. Chem. Phys.* 124, 154709 (2006)]. *The Journal of Chemical Physics* 125, 249901.
- Persson, K., Bengtson, A., Ceder, Gerbrand, Morgan, D., 2006. Ab initio study of the composition dependence of the pressure-induced spin transition in the $(\text{Mg}_{1-x}, \text{Fe}_x)\text{O}$ system. *Geophysical Research Letters* 33, L16306.
- Pownceby, M.I., O'Neil, H.S.C., 1994. Thermodynamic data from redox reactions at high temperatures. IV. Calibration of the Re-ReO₂ oxygen buffer from EMF and NiO plus Ni-Pd redox sensor measurements. *Contributions to Mineralogy and Petrology* 118, 130–137.
- Sha, X., Cohen, R.E., 2010. First-principles thermal equation of state and thermoelasticity of hcp Fe at high pressures. *Physical Review B* 81, 094105.
- Shim, S.-H., 2008. The Postperovskite Transition. *Annual Review of Earth and Planetary Sciences* 36, 569–599.
- Sinmyo, R., Ozawa, H., Hirose, K., Yasuhara, a., Endo, N., Sata, N., Ohishi, Y., 2008. Ferric iron content in $(\text{Mg,Fe})\text{SiO}_3$ perovskite and post-perovskite at deep lower mantle conditions. *American Mineralogist* 93, 1899–1902.
- Speziale, S., Zha, C.S., Duffy, T.S., Hemley, R. J., Mao, H., 2001. Quasi-hydrostatic compression of magnesium oxide to 52 GPa: Implications for the pressure-volume-temperature equation of states. *Journal of Geophysical Research* 106, 515–528.
- Sturhahn, Wolfgang, 2005. The spin state of iron in minerals of Earth's lower mantle. *Geophysical Research Letters* 32, L12307.
- Tange, Y., Takahashi E., Nishihara Y., Funakoshi K., Sata N., 2009. Phase relations in the system MgO-FeO-SiO_2 to 50 GPa and 2000 °C: An application of experimental techniques using multi-anvil apparatus with sintered diamond anvils, *Journal of Geophysical Research* 114, B02214,
- Tange, Y., Kuwayama, Y., Irifune, T., Funakoshi, K., Ohishi, Yasuo, 2012. P-V-T equation of state of MgSiO_3 perovskite based on the MgO pressure scale: A comprehensive reference for mineralogy of the lower mantle. *Journal of Geophysical Research* 117, B06201.

- Tateno, S., Hirose, K., Sata, N., Ohishi Y., 2009. Determination of post-perovskite phase transition boundary up to 4400 K and implications for thermal structure in D'' layer. *Earth and Planetary Science Letters*, 277, 130–136.
- Tsuchiya, T., Wentzcovitch, R., Da Silva, C., De Gironcoli, S., 2006. Spin Transition in Magnesiowüstite in Earth's Lower Mantle. *Physical Review Letters* 96, 1–4.
- Wang, L., Maxisch, T., Ceder, Gerbrand, 2006. Oxidation energies of transition metal oxides within the GGA+U framework. *Physical Review B* 73, 195107.
- Wentzcovitch, R M, Justo, J.F., Wu, Z., Da Silva, C.R.S., Yuen, D. a, Kohlstedt, D., 2009. Anomalous compressibility of ferropericlase throughout the iron spin crossover. *Proceedings of the National Academy of Sciences of the United States of America* 106, 8447–8452.
- Wood, B.J., Walter, M.J., Wade, J., 2006. Accretion of the Earth and segregation of its core. *Nature*, 441, 825-833.
- Xu, W., Bertelloni, C.L., Stixrude L., Ritsema, J., 2008. The effect of bulk composition and temperature on mantle seismic structure. *Earth and Planetary Science Letters* 275, 70-79.
- Zhang, F., Oganov, A.R., 2006. Valence state and spin transitions of iron in Earth's mantle silicates. *Earth and Planetary Science Letters* 249, 436–443.

Supplemental Information:

1. $fO_2(T,P)$ of different capsules

The modeling in this work requires knowing the fO_2 in different capsules (Re-ReO₂, diamond) and under lower mantle conditions at different temperatures and pressures. From the work of (Campbell et al., 2007), we can obtain the Re-ReO₂ capsule isothermal fO_2 at $P=0\text{GPa}$, 20GPa , 40GPa for $T=1500\text{K}$ and 2000K . However, we have to develop a method to extrapolate the fO_2 up to 120GPa and to $T=3000\text{K}$ and 4000K .

Following (Campbell et al., 2009), for an oxidation reaction of the form



the effect of pressure on fO_2 depends on the volume difference (ΔV) between oxide and metal through

$$\left. \frac{\partial \ln[f(O_2)]}{\partial P} \right|_T = \frac{2}{xRT} \Delta V \quad (\text{S2})$$

Eq. (S2) here correspond to the Eq. (3) in (Campbell et al., 2009).

In another section of (Campbell et al., 2007), the $\Delta V(P)$ curve of the [ReO₂-Re] pair is shown and it is clear that $\Delta V(P)$ is well-approximated by a linear function of P at a given temperature. We therefore assume we can write

$$\Delta V(P) = A \times P + B \quad (\text{S3})$$

where A and B are undetermined constants. Integrating Eq. (S2) with the form in Eq. (S3) yields

$$\ln[f(O_2)]_T = A_1 \times P^2 + B_1 \times P + C_1 \quad (\text{S4})$$

which has three undetermined parameters, A_1 , B_1 , and C_1 . We can now use the values for fO_2 at $P=0$, 20 and 40GPa on the $T=2000\text{K}$ isothermal line to fit the A_1 , B_1 and C_1 . We then use this fitted expression to extrapolate the fO_2 at higher pressures.

For the temperature dependence we take a similar approach, noting that there is an approximately linear relationship between $\ln[f(O_2)]$ and $1/T$ at a fixed pressure for a

metal-metal oxide pair according to Fig 6. (a) and (b) in (Campbell et al., 2009).

Therefore, at a certain pressure, we can approximate:

$$\ln[f(O_2)]_T = A_1 \times P^2 + B_1 \times P + C_1 \quad (S5)$$

where A_2 and B_2 are undetermined constant. As we already have the fO_2 of Re-ReO₂ capsule at $T=1500K$ and $T=2000K$, it is straightforward to extrapolate to higher temperatures.

We can now use these expressions as a guide to find the general expression of $\text{Log}[f(O_2)]$ as a function of T and P . As the $\text{Log}[f(O_2)]_P$ is a linear function of $1/T$, for convenience we write $\text{Log}[f(O_2)](P, 1/T)$ and consider a Taylor expansion around $P=0$ and $1/T=0$ (to third order) as:

$$\begin{aligned} \text{Log}[f(O_2)](P, \frac{1}{T}) = & L_0 + L_1 \times P + L_2 \times \frac{1}{T} + L_3 \times P^2 + L_4 \times \frac{P}{T} + L_5 \times \frac{1}{T^2} + L_6 \times P^3 + L_7 \times \frac{P^2}{T} + \\ & L_8 \times \frac{P}{T^2} + L_9 \times \frac{1}{T^3} \end{aligned} \quad (S6)$$

Based on equation S4 and S5, we can accurately represent P and $1/T$ dependence without terms of the form P^3 , $(1/T)^2$ and $(1/T)^3$. Therefore, we can take L_5 , L_6 , L_8 and L_9 in S6 as equal to zero. Rewriting Eq. (S6) with this further approximation yields:

$$\text{Log}[f(O_2)](P, \frac{1}{T}) = L_0 + L_1 \times P + L_2 \times \frac{1}{T} + L_3 \times P^2 + L_4 \times \frac{P}{T} + L_7 \times \frac{P^2}{T} \quad (S7)$$

Eq. (S7) has six unknowns and we have experimental data of $\text{Log}[f(O_2)]$ at $P = (0GPa, 20GPa, 40GPa)$ and $T = (1500K, 2000K)$, which gives us six data points for fitting, so a simple regression fit will yield the unknown G values. We find that for a fit with P in GPa and T in 1000K (or $1/T$ in units of $1000/T$, so at $T=1000K$ we have $1/T = 1$, $T=2000K$ we have $1/T=0.5$, etc.) we get:

$$\text{Log}[f(\text{O}_2)](P, \frac{1}{T}) = 7.1 + 1.75 \times 10^{-2} \times P + (-24) \times \frac{1}{T} + 1.25 \times 10^{-4} \times P^2 + 0.57 \times \frac{P}{T} + (-1.5 \times 10^{-3}) \times \frac{P^2}{T} \quad (\text{S8})$$

The data used for fitting and the fitted parameters and the are shown in Table S1 and the values used for the thermodynamic model are shown in Table S2:

		Log[$f\text{O}_2$] data used for fitting	
$P \backslash T$		1500 K	2000 K
0 GPa		-8.9	-4.9
20 GPa		-1.3	0.9
40 GPa		5.6	6.2

Table S1. The data of Log[$f\text{O}_2$] used for fitting our Log[$f\text{O}_2$] model.

$P \backslash T$	2000 K	3000 K	4000 K
20 GPa	0.9	3.1	4.2
30 GPa	3.61	4.97	5.66
40 GPa	6.2	6.8	7.1
50 GPa	8.66	8.54	8.48
60 GPa	11	10.2	9.8
70 GPa	13.21	11.79	11.1
80 GPa	15.3	13.3	12.3
90 GPa	17.26	14.74	13.48
100 GPa	19.1	16.1	14.6
110 GPa	20.82	17.39	15.68
120 GPa	22.4	18.6	16.7

Table S2. Log[$f\text{O}_2$] of Re-ReO₂ capsule in lower mantle T and P range.

After we have a model for the Log[$f(\text{O}_2)$] value of the Re-ReO₂ capsule, the next step is trying to find the relation between Re-ReO₂ capsule and other capsules. The $f\text{O}_2$ in the

diamond capsule is about 4 orders of magnitude lower than the Re-ReO₂ at 25GPa, 2000K (Pownceby and O'Neil, 1994). We assume that within the pressure and temperature range of our thermodynamic model (P : 20~120GPa, T : 2000~4000K), the diamond capsule f_{O_2} is always 4 orders of magnitude lower than the Re-ReO₂ capsule f_{O_2} . We also make a quick estimation of the effect of this assumption, if we vary the diamond capsule f_{O_2} by ± 2 order of magnitude, at $T=2000K$, the reaction energy change of Eq. (1) is about $\pm 0.19eV/Fe$. The corresponding $Fe^{3+}/\Sigma Fe$ difference is about +0.14 and -0.07 for $T=2000K$, diamond capsule case. Qualitatively this variance doesn't change the fact that the Fe^{3+} fraction is small (0~0.35 within the lower mantle pressure range) in diamond capsule at $T=2000K$. And we still have the fact that the $Fe^{3+}/\Sigma Fe$ in diamond capsule is lower than that in Re-ReO₂ capsule. Therefore in our thermodynamic model, we use $(Log[f(O_2)]|_{Re-ReO_2} - 4)$ as the f_{O_2} input for the diamond capsule and we believe that likely deviations from this assumption will not have a qualitative effect on our results.

These relationships provide at least approximate models for the f_{O_2} for all the necessary conditions for the thermodynamic modeling in this work.

2. Integrated model details

Here we describe how we combine the oxidation reaction model and chg. disp. reaction model together. The approach is the same as with the models treated separately. Consider the equilibration process by starting with one mole of $(\text{Mg}_{1-x}\text{Fe}_x)\text{SiO}_3$. When the system comes into equilibrium, n_1 mole of ferrous Mg-Pv is transferred to ferric Mg-Pv through the oxidation reaction and n_2 mole of ferrous Mg-Pv is transferred to ferric Mg-Pv through the chg. disp. reaction. Then the compact form for the whole system is:

$$\left(1 + \frac{1}{2}n_1x + \frac{1}{3}n_2x\right) \left(\text{Mg}_{\frac{1-(1-n_1-n_2)x}{1+\frac{1}{2}n_1x+\frac{1}{3}n_2x}} \text{Fe}_{\frac{2+(1-n_1-n_2)x}{1+\frac{1}{2}n_1x+\frac{1}{3}n_2x}}^{2+} \text{Fe}_{\frac{3+n_1x/2+n_2x/3}{1+\frac{1}{2}n_1x+\frac{1}{3}n_2x}}^{3+}} \right) \left(\text{Si}_{\frac{1}{1+\frac{1}{2}n_1x+\frac{1}{3}n_2x}} \text{Fe}_{\frac{3+\text{HS}}{1+\frac{1}{2}n_1x+\frac{1}{3}n_2x}}^{3+} \text{Fe}_{\frac{3+\text{LS}}{1+\frac{1}{2}n_1x+\frac{1}{3}n_2x}}^{3+}} \right) \text{O}_3 + \frac{1}{4}(1-n_1)x\text{O}_2 + (1-n_1-n_2)x\text{MgO} + \frac{n_2x}{3}\text{Fe}^0 \quad (\text{S9})$$

We take the total Fe content as $x = 1/8$ and y is the B-site HS Fe^{3+} ratio. As done for the oxidation reaction and chg. disp. reaction separately, we can use Eq. S9 to write the expression of total Gibbs energy $G(n_1, n_2, y; P, T)$. The expression of total Gibbs energy in the integrated model is:

$$G_{\text{Total}} = (1-n_1-n_2)H[(\text{Mg}_{1-x}\text{Fe}_x)\text{SiO}_3] + \left(\frac{n_1}{2} + \frac{n_2}{3}\right)yH[(\text{Mg}_{1-x}\text{Fe}_x)\left(\text{Si}_{1-x}\text{Fe}_x^{\text{HS}}\right)\text{O}_3] + \left(\frac{n_1}{2} + \frac{n_2}{3}\right)(1-y)H[(\text{Mg}_{1-x}\text{Fe}_x)\left(\text{Si}_{1-x}\text{Fe}_x^{\text{LS}}\right)\text{O}_3] + (1-n_1-n_2)H[\text{MgO}] + \frac{1}{4}(1-n_1)\mu(\text{O}_2) + \frac{xn_2}{3}H[\text{Fe}] - (1-n_1-n_2)xTS_{\text{mag}}(\text{Fe}^{2+}, A) - \left(\frac{n_1}{2} + \frac{n_2}{3}\right)xTS_{\text{mag}}(\text{Fe}^{3+}, A) - \left(\frac{n_1}{2} + \frac{n_2}{3}\right)xyTS_{\text{mag}}(\text{Fe}^{3+\text{HS}}, B) - \left(\frac{n_1}{2} + \frac{n_2}{3}\right)x(1-y)TS_{\text{mag}}(\text{Fe}^{3+\text{LS}}, B) - \frac{xn_2}{3}TS[\text{Fe}^0] - \left(1 + \frac{n_1x}{2} + \frac{n_2x}{3}\right)TS_{\text{conf}}(A) - \left(1 + \frac{n_1x}{2} + \frac{n_2x}{3}\right)TS_{\text{conf}}(B) \quad (\text{S10})$$

where G_{Total} is the total Gibbs energy for the system with states associated with both the oxidation and chg. disp. reactions. The definitions of the enthalpy terms and the magnetic entropy terms are consistent with those in the oxidation reaction model. The configurational entropy terms in sublattices A and B are:

$$S_{\text{config}}(A) = k_B \left[\frac{1-(1-n_1-n_2)x}{1+\frac{n_1}{2}x+\frac{n_2}{3}x} \ln\left(\frac{1-(1-n_1-n_2)x}{1+\frac{n_1}{2}x+\frac{n_2}{3}x}\right) + \frac{(1-n_1-n_2)x}{1+\frac{n_1}{2}x+\frac{n_2}{3}x} \ln\left(\frac{(1-n_1-n_2)x}{1+\frac{n_1}{2}x+\frac{n_2}{3}x}\right) + \frac{\left(\frac{n_1}{2} + \frac{n_2}{3}\right)x}{1+\frac{n_1}{2}x+\frac{n_2}{3}x} \ln\left(\frac{\left(\frac{n_1}{2} + \frac{n_2}{3}\right)x}{1+\frac{n_1}{2}x+\frac{n_2}{3}x}\right) \right]$$

$$\begin{aligned}
S_{\text{config}}(B) = k_B [& \frac{1}{1 + \frac{n_1}{2}x + \frac{n_2}{3}x} \ln\left(\frac{1}{1 + \frac{n_1}{2}x + \frac{n_2}{3}x}\right) + \frac{y(\frac{n_1}{2}x + \frac{n_2}{3}x)}{1 + \frac{n_1}{2}x + \frac{n_2}{3}x} \ln\left(\frac{y(\frac{n_1}{2}x + \frac{n_2}{3}x)}{1 + \frac{n_1}{2}x + \frac{n_2}{3}x}\right) + \\
& \frac{(1-y)(\frac{n_1}{2}x + \frac{n_2}{3}x)}{1 + \frac{n_1}{2}x + \frac{n_2}{3}x} \ln\left(\frac{(1-y)(\frac{n_1}{2}x + \frac{n_2}{3}x)}{1 + \frac{n_1}{2}x + \frac{n_2}{3}x}\right)]
\end{aligned}
\tag{S11}$$

We can obtain values for n_1 , n_2 , and y by simultaneously minimizing G_{TotalAll} with respect

to these variables. Note that $\frac{\partial G}{\partial y}$ is independent of n_1 and n_2 , which is consistent with the fact that the fraction of HS vs. LS B-site Fe^{3+} does not depend on the extent of the chg. disp. reaction.

3. DFT setup information and EOS comparison

This SI section contains further details of our density functional theory calculation approach. The endmembers of our system are ferrous Mg-Pv ($\text{Mg}_{1-x}\text{Fe}_x$) SiO_3 (where $x = 1/8$), ferric Mg-Pv ($\text{Mg}_{1-x_1}\text{Fe}_{x_1}$)($\text{Si}_{1-x_1}\text{Fe}_{x_1}$) O_3 (where $x_1 = 1/17$ in the oxidation reaction model and $x_1 = 1/25$ in the chg. disp. reaction), pure Mg-Pv, MgO, and metallic Fe. As our model assumes that Fe can be treated as weakly interacting on a given sublattice we attempt to obtain a consistent set of energetics by estimating the energy for maximally isolated Fe on each sublattice. We therefore use a 120 atom supercell for all the Mg-Pv structures with at most just one Fe atom on each sublattice, which are ($\text{Mg}_{23}\text{Fe}_1$)(Si_{24}) O_{72} for ferrous Mg-Pv and ($\text{Mg}_{23}\text{Fe}_1$)($\text{Si}_{23}\text{Fe}_1$) O_{72} for ferric Mg-Pv. All the details of k points and symmetry information are shown in **Table S3**. The choices of k point mesh yield a convergence of total reaction energy better than 10 meV/Fe. Structural relaxation is set to converge to 10^{-3} eV in the total energy, yielding the average forces between atoms to be about 0.01 eV/Å.

	DFT set up information			
	Number of atoms	k-points	space group	Calculated lattice constant (20 GPa) (Ang) axbxc
MgO	2	5x5x5	Fm $\bar{3}$ m	2.04 (Mg-O bond)
$\text{Mg}_{24}\text{Si}_{24}\text{O}_{72}$	120	1x1x2	Pnma	9.31 x 14.49 x 6.73
($\text{Mg}_{23}\text{Fe}_1$) $\text{Si}_{24}\text{O}_{72}$	120	1x1x2	Pnma	9.31 x 14.50 x 6.74
($\text{Mg}_{23}\text{Fe}_1$)($\text{Si}_{23}\text{Fe}_1$) O_{72} HH	120	1x1x2	Pnma	9.32 x 14.55 x 6.76
($\text{Mg}_{23}\text{Fe}_1$)($\text{Si}_{23}\text{Fe}_1$) O_{72} HL	120	1x1x2	Pnma	9.31 x 14.52 x 6.75
Metallic hcp Fe	2	5x5x5	P6 ₃ /mmc	a=2.62 c=4.4 (0GPa)

Table S3. The ab initio parameters used for the compounds in our model. We use experimental EOS for the metallic hcp Fe combined with the DFT calculation at $P = 0$ GPa, so we show the calculated lattice constant of hcp Fe at 0 GPa here. “HH” means high spin in both A and B sites for ferric Mg-Pv and “HL” means high spin in A site and low spin in B site.

For the Fe^{3+} - Fe^{3+} coupled ferric Mg-Pv, we use a ($\text{Mg}_{23}\text{Fe}_1$)($\text{Si}_{23}\text{Fe}_1$) O_{72} supercell with one Fe in the A site and the other Fe in the B site. The two Fe atoms are placed as

neighbors to obtain a configuration with the lowest energy (Zhang and Oganov, 2006). We also have two different spin states for the ferric Mg-Pv. At relatively low pressures, the coupled Fe^{3+} - Fe^{3+} is in the high-spin and high-spin (HS-HS) state. When the pressure increases, the ferric Mg-Pv will gradually change to a high-spin and low-spin (HS-LS) state. The HS-HS corresponds to the state with $5\mu_B$ and $5\mu_B$ of magnetic moment on the A site and B site respectively. The HS-LS is the state with $5\mu_B$ and $1\mu_B$ on the A site and B site.

To validate the accuracy of our ab-initio calculation of these high pressure phases, we compare the calculated equation of state (EOS) parameters (V_0, K_0, K_0') of all the endmembers in our thermodynamic model with experiments. The comparison is shown in **Table. S4**. For V_0 , the relative difference ($|V_{0,exp} - V_{0,sim}|/V_{0,exp}$) in all the cases is less than 0.5% and calculated values are typically smaller. The zero pressure bulk modulus relative difference ($|K_{0,exp} - K_{0,sim}|/K_{0,exp}$) in all the cases is less than 3.5%. We note that our DFT results are at 0 K, but the experimental results correspond to 300 K. So we need to consider the thermal effects on volume and bulk modulus. At room temperature and 1 bar condition, the thermal expansion coefficient, $\alpha = \frac{1}{V}(\frac{dV}{dT})_p$, and temperature derivative of bulk modulus K with respect to pressure, $(\frac{dK}{dT})_p$, are: (1) for Mg-Pv, $\alpha = 2.5 \times 10^{-5}/\text{K}$ (Tange et al., 2012), $(\frac{dK}{dT})_p = -0.017 \text{ GPa/K}$ (Fiquet et al., 2000). (2) for MgO, $\alpha = 3.56 \times 10^{-5}/\text{K}$ and $(\frac{dK}{dT})_p = -0.015 \text{ GPa/K}$ (Mao et al., 2011a). These thermal expansions are not fit to low temperatures below the Debye temperature but should provide an upper bound for the scale of changes we are likely to see in these materials from 0 to 300 K. With temperature difference $\Delta T = 300 \text{ K}$ the thermal effect on volume is about 0.75% change for Mg-Pv and 1% change for MgO, and the thermal effect on bulk modulus is about 2% change for Mg-Pv, 3% change for MgO. So the temperature effect (from 0 to 300 K) is expected to be close to or within our simulation uncertainties. Based on the above discussion, our calculated EOS parameters are in good agreement with those from experiments, which overall gives us confidence in the validity of our DFT energetics.

	Simulation				Experiment			
	V ₀ (Å ³)/f.u.	K ₀ (GPa)	K ₀ '	Fe % /site	V ₀ (Å ³)/f.u.	K ₀ (GPa)	K ₀ '	Fe % /site
MgO	18.62	166.7	4.15	N/A	18.67 ^a	160 ^b	4 ^b	N/A
Mg ₂₄ Si ₂₄ O ₇₂	40.5	256.14	4.02	N/A	40.58 ^c	261 ^c	4 ^c	N/A
(Mg ₂₃ Fe ₁)Si ₂₄ O ₇₂	40.58	255.04	4.06	4.2%	40.65 ^c	260.4 ^c	4 ^c	4.2%
(Mg ₂₃ Fe ₁)(Si ₂₃ Fe ₁)O ₇₂ HH	40.93	252.02	4.04	4.2%	41.00 ^d	249.23 ^d	4 ^d	4.2%
(Mg ₂₃ Fe ₁)(Si ₂₃ Fe ₁)O ₇₂ HL	40.59	271.2	3.69	4.2%	40.42 ^d	282.08 ^d	4 ^d	4.2%
Metallic hcp Fe	—	—	—	N/A	11.19 ^e	156 ^e	5.81 ^e	N/A

^a (Jacobsen et al., 2002)

^b (Speziale et al., 2001)

^c (Lundin et al., 2008)

^d (Catalli et al., 2010)

^e (Dubrovinsky et al., 2000)

Table S4. Fitted 3rd-order Birch-Murnaghan EOS parameters of all the compounds in the ab-initio based thermodynamic model (fit over a pressure range of -10GPa to 120GPa), compared to the results of experiments. “/f.u.” means per formula unit, and for all the Mg-Pv endmembers one f.u. corresponds to one A, one B, and 3 O sites (a 5-site ABO₃ unit cell). “HH” means high spin in both A and B sites for ferric Mg-Pv and “HL” means high spin in A site and low spin in B site. As we take experimental EOS parameters for the metallic Fe in our thermodynamic model, we don’t show the simulated values for these parameters of metallic Fe.

For the metallic Fe, experiments show that the stable phase in the lower mantle pressure range is hcp in a non-magnetic state (Mathon et al., 2004). However, there is presently a disagreement about the electronic structure of Fe between simulations and experiments (Sha and Cohen, 2010). Furthermore, the EOS of hcp Fe at high pressure by simulation does not match well with experiments. Therefore, in this work, we use only the ab initio energy for hcp metallic Fe at 0 GPa and otherwise use the experimental Birch-Murnaghan third order equation of state parameters for metallic Fe (Dubrovinsky et al., 2000), which are given in **Table S4**. For the ab-initio energy of hcp metallic Fe at 0 GPa,

we use the lowest energy state (ground state) value, which is the 0 GPa energy of ferromagnetic hcp metallic Fe. With our ab initio energy and this EOS we can calculate the enthalpy of Fe at any given pressure.

We have chosen not to use the more commonly applied DFT+ U (Anisimov et al., 1991) method for treating these particularly correlated transition metal oxide systems. DFT+ U has been used for a wide-range of studies of Fe in geophysical studies, including in both (Mg,Fe)O ferropericlase (Persson et al., 2006; Tsuchiya et al., 2006; Wentzcovitch et al., 2009) and Mg-Pv (Bengtson et al., 2008; Hsu et al., 2011, 2010; Metsue and Tsuchiya, 2012). However, while U can be determined by self-consistent ab initio methods, such calculations for Fe in ferropericlase and Mg-Pv have shown wide variation in U values for Fe depending on site, valence, spin state and pressure (Hsu et al., 2011, 2010; Tsuchiya et al., 2006), with values ranging from 3 to 5 eV for the different possible Fe states in just Mg-Pv (Hsu et al., 2011, 2010). Given the many environments and the wide range of pressures required to treat Fe in this work, including metallic Fe⁰, the hybrid HSE06 functional appeared to provide a simpler approach, without a large set of U values to establish. To assure that our results were not completely different with the two methods we studied the chg. disp. reaction (Eq. (9)) with the GGA+ U method using self-consistent U values for A and B sites taken from Hsu et al. (2011, 2010). These results found a $\Delta H = 400$ meV/Fe, comparable to the value of 500 meV/Fe for the HSE results shown in this work. We also note that our spin transition pressure, discussed in section 3.2, matches closely with previous LDA+ U calculations. Therefore, we believe that similar results as those presented here could also be obtained by careful application of varied self-consistent U 's, although that method was not pursued here.

4. Impact of Fe partitioning

In this section we consider the potential impact of partitioning of Fe between Mg-Pv and ferropericlasite (Fp) on our predictions for $\text{Fe}^{3+}/\Sigma\text{Fe}$ in Mg-Pv. We will split the problem into two parts: (a) at high $f\text{O}_2$, only oxidation reaction occurs in the system; (b) at low $f\text{O}_2$, we will study what is the $f\text{O}_2$ level when chg. disp. reaction suppresses oxidation reaction.

4.1 At high $f\text{O}_2$

As the oxidation reaction is the dominant reaction at high $f\text{O}_2$ condition (by which we mean $f\text{O}_2$ higher than the $f\text{O}_2^t$ identified in section 3.1, we don't need to consider the chg. disp. reaction. If some amount of Fe partitions from Mg-Pv to Fp, two effects may change the $\text{Fe}^{3+}/\Sigma\text{Fe}$ calculated from Mg-Pv coexisting with pure MgO model (Eq. 1 and Eq. 9).

First, the effective chemical potential of MgO is lowered if we have some Fe in the Mg site. If we assume that the FeO and MgO mix as an ideal solution in Fp, the effective chemical potential of MgO in $(\text{Mg}_{1-x}\text{Fe}_x)\text{O}$ can be estimated as:

$$\mu^{\text{eff}}(\text{MgO}) = \mu^0(\text{MgO}) + k_B T \ln(1-x) \quad (\text{S12})$$

In the lower mantle, the Fe in Fp is about $x=0.2$ (Hirose, 2002). Here we will show $\text{Fe}^{3+}/\Sigma\text{Fe}$ in Mg-Pv when Fe in Fp is $x = 0.1, 0.2,$ and 0.3 to assess the influence of MgO chemical potential changes from Fe partitioning into MgO. The results are shown in Fig. S1, where the predictions have been made with Eq. 1 with the MgO chemical potential modified by Eq. S12. We can see that there is no significant change of $\text{Fe}^{3+}/\Sigma\text{Fe}$ in Mg-Pv. Even when the Fe in Fp is $x = 0.3$, the largest decrease of $\text{Fe}^{3+}/\Sigma\text{Fe}$ in Mg-Pv is less than 0.08. Therefore our reactions (Eq. 1) with pure MgO as the reactants give qualitatively and even semiquantitatively the correct values for what would be obtained with equilibrium with $(\text{Mg,Fe})\text{O}$.

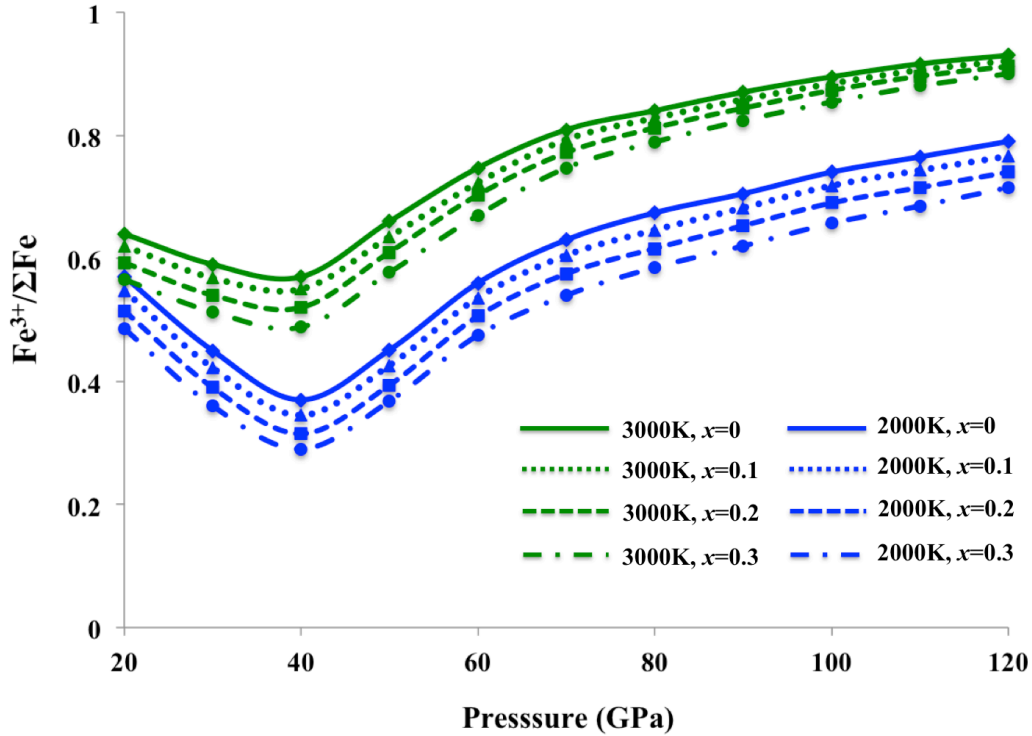


Fig. S1 $\text{Fe}^{3+}/\Sigma\text{Fe}$ in Mg-Pv at Re-ReO₂ capsule $f\text{O}_2$ condition when Fe% in Fp is 10, 20 and 30. The blue curves correspond to $T=2000\text{K}$, the green curve correspond to $T=3000\text{K}$. The solid lines are the original $\text{Fe}^{3+}/\Sigma\text{Fe}$ curves when Fe content in $(\text{Mg}_{1-x}\text{Fe}_x)\text{O}$ is $x = 0$. The dotted lines, dashed lines and dotted-dashed lines correspond to Fe content in Fp of $x = 0.1, 0.2,$ and $0.3,$ respectively.

A second effect due to the Fe partitioning between Mg-Pv and Fp is that the total Fe content in Mg-Pv might vary. Here we show that the variation of $\text{Fe}^{3+}/\Sigma\text{Fe}$ in Mg-Pv arising from a change of Fe content in Mg-Pv is quite small and can be neglected. Table S5 shows the result of $\text{Fe}^{3+}/\Sigma\text{Fe}$ at different Fe% in Mg-Pv and different temperature and pressure conditions. These results indicate that although the Fe partitioning between Mg-Pv and Fp may alter the total Fe content in Mg-Pv, the $\text{Fe}^{3+}/\Sigma\text{Fe}$ ratio predicted from our thermodynamic model changes by less than 10% over a very large range of Mg-Pv Fe content. These results show that our results for $\text{Fe}^{3+}/\Sigma\text{Fe}$ ratio in Mg-Pv are quite general for different Fe in Mg-Pv compositions and, in particular, support that we can neglect effects of Fe partitioning in the model.

Total Fe% in Mg-Pv	Fe ³⁺ /ΣFe in Mg-Pv			
	T=2000K		T=3000K	
	40GPa	100GPa	40GPa	100GPa
1%	0.35	0.697	0.558	0.879
5%	0.362	0.725	0.565	0.891
12.5%	0.37	0.74	0.575	0.895
20%	0.39	0.75	0.591	0.903

Table. S5 The dependence of Fe³⁺/ΣFe on the total Fe content in Mg-Pv at different pressure and temperature conditions. 40GPa represents relatively low pressures region. 100GPa represents relatively high pressures region. The result of total Fe% in Mg-Pv=12.5% corresponds to the prediction of our model in the main text.

4.2 At low fO_2

When the fO_2 goes lower than the fO_2^t value discussed in section 3.1 the influence on the Fe³⁺/ΣFe ratio in Mg-Pv due to Fe partitioning is similar to that shown above. Now we only need to consider chg. disp. reaction (Eq. 9). We still have two effects that may change the Fe³⁺/ΣFe ratio in Mg-Pv when we consider the Fe partitioning. First, the effective chemical potential of MgO is lowered, which is shown in Eq. S12. Second, the Fe content in Mg-Pv may change. The impact of these two effects on the chg. disp. reaction should be similar to that on the oxidation reaction, which has already been discussed in SI section 4.1. The general conclusion is that the Fe partitioning also doesn't significant change the Fe³⁺/ΣFe in Mg-Pv contributed from chg. disp. reaction. To consider the fO_2 transition point between chg. disp. reaction and oxidation reaction, please refer to the discussion in the section 3.1 and the details shown in SI section 5.

5. Ideal solution model of Fe⁰-ferropericlase equilibrium fO_2

The possible range of the Fe⁰-ferropericlase (Fp) equilibrium fO_2 (shown in the grey box in Fig.1) is derived from experimental data and an ideal solution model. We model Fe-FeO capsule relative to Re-ReO₂ capsule following the previous experimental evidence suggesting that the fO_2 of Fe-FeO capsule is about 6 order of magnitude lower than that of Re-ReO₂ capsule (Frost et al., 2004). We then further modify the $\mu(Fe^{2+})$ to correct the fact that the FeO is dissolved in MgO to form the Fp. Based on the reaction $2Fe^0 + O_2 \rightarrow 2Fe^{2+}O$ and the expression of $\mu(Fe^{2+})$ in (Mg_{1-x}Fe_x)O: $\mu(Fe^{2+}) = \mu(Fe^{2+})_{FeO} + kT \ln x$ (ideal solution model) we can easily calculate the fO_2 shift relative to Fe-FeO level at a certain Fe concentration in ferropericlase.

First, we define the equilibrium fO_2 of Fe-FeO system as $fO_2[Fe-FeO]$. Then we have the equation:

$$2 \mu(Fe^0) + \mu_{O_2} + kT \ln fO_2[Fe-FeO] = 2 \mu(FeO) \quad (S13)$$

If the system is at $P=100\text{GPa}$, $T=2000\text{K}$ which is consistent with the condition in Fig. 1, $\mu(Fe^0)$ is the chemical potential of metallic Fe at (100GPa, 2000K), $\mu(FeO)$ is the chemical potential of FeO at (100GPa, 2000K), μ_{O_2} is the reference chemical potential of O₂ when partial pressure of O₂ is 1atm at $T=2000\text{K}$.

Then we define the equilibrium fO_2 of Fe- (Mg_{1-x}Fe_x)O system as $fO_2[(Mg_{1-x}Fe_x)O]$. Then we have the equation:

$$2 \mu(Fe^0) + \mu_{O_2} + kT \ln fO_2[(Mg_{1-x}Fe_x)O] = 2 (\mu(FeO) + kT \ln x) \quad (S14)$$

Then we do (Eq. S14) – (Eq. S13), it yields the following expression:

$$\text{Log}[fO_2[(Mg_{1-x}Fe_x)O]] = \text{Log}[fO_2[Fe-FeO]] + 2 \text{Log}x = fO_2[Re-ReO_2-6] + 2 \text{Log}x \quad (S15)$$

With Eq. S15, we are able to create the grey box shown in Fig. 1 which tells us the range of the equilibrium fO_2 of (Mg_{1-x}Fe_x)O where x is from 0.05 to 0.4.

Erratum for the Paper “*Origin of Fe³⁺ in Fe-containing, Al-free Mantle Silicate Perovskite*”

Shenzhen Xu¹, Sang-Heon Shim³, Dane Morgan^{1,2}

¹*Materials Science Program*

²*Department of Materials Science and Engineering*

University of Wisconsin – Madison, Madison, WI

³*School of Earth and Space Exploration*

Arizona State University, Tempe, AZ

Corresponding author (Dane Morgan): Telephone: +1-608-265-5879; Fax: +1-608-262-8353;

Email: ddmorgan@wisc.edu

In the main text section 2.1.1 the term $H_{\text{vib}}^0(\text{O}^{2-}_{\text{solid}})$ in the equation for $G_{\text{vib}}(\text{O}^{2-}_{\text{solid}}) - H_{\text{vib}}^0(\text{O}^{2-}_{\text{solid}})$ was miscalculated. The incorrect value was 0.63eV and the corrected value is 0.095eV. As discussed below, this correction demonstrated that there was some discrepancy in the DFT oxidation energies, so we now add another correction term with an increase $\mu(\text{O}_2)$ in main text eq. (4) by 0.4eV/O₂. These corrections change the reaction energy of Eq. (1), and have the effect of stabilizing oxygen gas and reducing the amount of Fe³⁺ created by oxidation. This change does not significantly impact the curve shapes, the qualitative conclusions, or the discussions, except regarding Fig. 1, which we detail below. Unfortunately, many of the specific values shown in the figures and mentioned in the text related to the oxidation reaction in Eq. (1) are somewhat changed, so below we give revised figures and specific corrections for regions of text or values which need to be updated. Figs. 1, 2, 4(a), and 5 in the main text are changed to the new Figs E1, E2, E4(a), and E5, respectively.

The changes to the text are: **Pg 323/lc(left column) ln(line) 11**, remove “We don’t use any data from FeO or ferropericlase in constructing our model, so being consistent with Fe⁰/ferropericlase equilibrium thermodynamics is an important test of the model.” **Pg 323/lc ln33**, remove “The ability to define this range consistently for both Mg-Pv and Fp, despite the model

being developed without any explicit *ab initio* calculations on the Fp system, supports the accuracy of our thermodynamic model.” **Pg 323/lc ln 25**, change “11.6” to “12.8”. **Pg 323/lc ln 33**, change “11.6” to “12.8”. **Pg 323/rc(right column) ln 22**, change “0.5” to “0.3”. **Pg 323/rc ln 22**, change “0.08” to “0.05”. **Pg 323/rc ln 24**, change “0.7” to “0.6”. **Pg 323/rc ln 24**, change “0.2” to “0.13”. **Pg 326/lc ln 9**, change “0.4-0.5” to “0.3-0.35”. **Pg 326/lc ln 9**, change “0.08-0.1” to “0.05”. **Pg 326/lc 2nd ln from the bottom**, change “0.05” to “0.03”. **Pg 326/rc ln 1**, change “0.17” to “0.035”. **Pg 326/rc ln 1**, change “0.1” to “0.045”. **Pg 326/rc ln 2**, change “0.89” to “0.19”. **Pg 326/rc ln 2**, change “0.52” to “0.24”.

Our correction to $H^0_{\text{vib}}(\text{O}^{2-}_{\text{solid}})$ changes the predicted transition oxygen fugacity, $f\text{O}_2^{\ddagger}$, which is where the charge disproportionation (chg. disp.) reaction ceases to occur and the oxidation reaction starts to occur. Specifically, in Fig. 1 (main text) $f\text{O}_2^{\ddagger}$ changes from $\log(f\text{O}_2^{\ddagger}) = \log(f\text{O}_2[\text{Re-ReO}]) - 6.9$ to $\log(f\text{O}_2^{\ddagger}) = \log(f\text{O}_2[\text{Re-ReO}]) - 4.7$. Because the bridgmanite (Pv) is in equilibrium with ferropericlase (Fp) (Mg,Fe)O the Fe from the chg. disp. reaction can only exist for oxygen fugacity less than $f\text{O}_2[\text{Fe-(Mg,Fe)O}]$. We show below that $f\text{O}_2[\text{Fe-(Mg,Fe)O}] = \log(f\text{O}_2[\text{Re-ReO}_2]) - 5.7$. This yields a final change in value from the incorrect value $\log(f\text{O}_2^{\ddagger}) = \log(f\text{O}_2[\text{Re-ReO}]) - 6.9$ to the correct value $\log(f\text{O}_2^{\ddagger}) = \log(f\text{O}_2[\text{Re-ReO}_2]) - 5.7$. So in our corrected Fig. E1, we can see the $\log(f\text{O}_2^{\ddagger})$ is at $\log(f\text{O}_2[\text{Re-ReO}_2]) - 5.7$. The determination of $\log(f\text{O}_2[\text{Fe-(Mg,Fe)O}])$ is as follows. We first consider relative difference between $f\text{O}_2[\text{Fe-FeO}]$ and $f\text{O}_2[\text{Re-ReO}_2]$ at $T=2000\text{K}$, $P=20\text{GPa}-100\text{GPa}$ (lower mantle relevant conditions) from experiments (Campbell et al., 2007; Campbell et al., 2009). The experimental results show that $\log(f\text{O}_2[\text{Fe-FeO}])$ is -4.5 to -5 with respect to $\log(f\text{O}_2[\text{Re-ReO}_2])$. We take an average which is -4.75~-4.8 to represent the $\log f\text{O}_2$ difference between Fe-FeO and Re-ReO₂. Now we consider the difference between $\log(f\text{O}_2[\text{Fe-FeO}])$ and $\log(f\text{O}_2[\text{Fe-(Mg,Fe)O}])$. In our model the Fe content in Pv is 0.125 per formula unit of MgSiO₃, which is (Mg_{0.875}Fe_{0.125})SiO₃. Based on previous experiments, the Fe partitioning coefficient K_D between Pv and Fp is 0.2-0.3 in Al-free condition (Irvine, 2010). If we take an average, then we can assume $K_D \approx 0.25$ in Al-free condition. Then

based on the definition of K_D ($K_D^{Pv-Fp} = (Fe/Mg)_{Pv} / (Fe/Mg)_{Fp}$), we can find that $(Mg_{0.875}Fe_{0.125})SiO_3$ should be in equilibrium with $(Mg_{0.64}Fe_{0.36})O$. Under an ideal solution approximation (SI section 5), $\log(fO_2[(Mg_{0.64}Fe_{0.36})O])$ is calculated to be -0.9 with respect to $\log(fO_2[Fe-FeO])$. Therefore based on above arguments, we have $\log(fO_2[Fe-(Mg,Fe)O]) = \log(fO_2[(Mg_{0.875}Fe_{0.125})SiO_3]) = \log(fO_2[(Mg_{0.64}Fe_{0.36})O]) = \log(fO_2[Fe-FeO]) - 0.9 = \log(fO_2[Re-ReO_2]) - 5.7$.

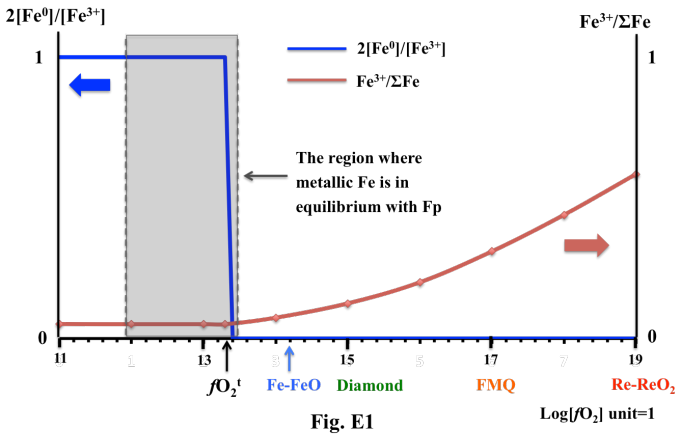


Fig. E1

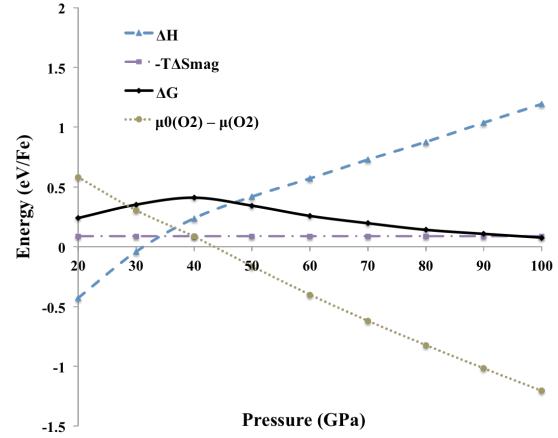
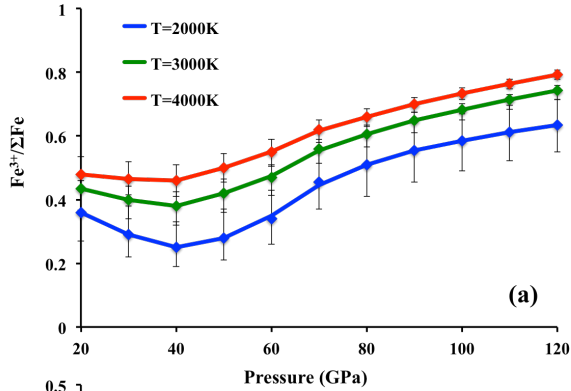
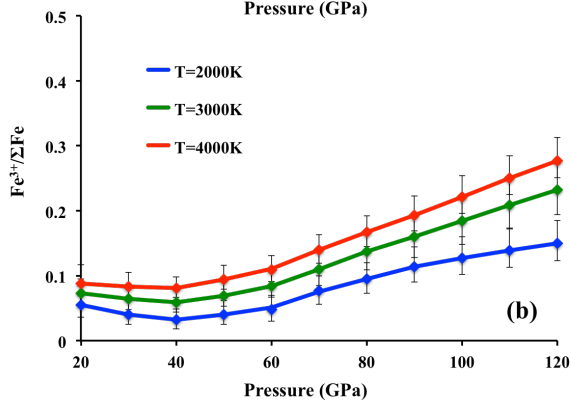


Fig. E4(a)



(a)



(b)

Fig. E2

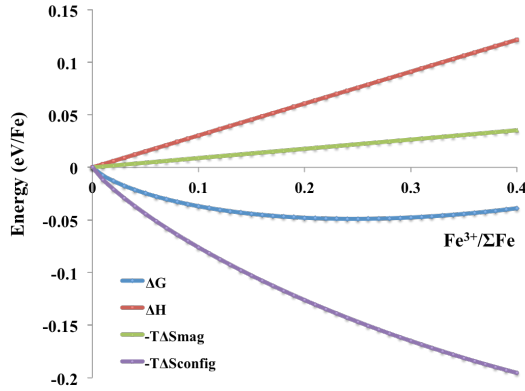


Fig. E5

References

Campbell, A.J., Daniel, L., Richter, K., Seagle, C.T., Wang, Y., Prakapenka, V., 2007. Pressure-Volume-Temperature study of metal-oxide pairs, 2007 COMPRESS Annual Meeting, Fairlee, Vermont.

Campbell, A.J., Danielson, L., Richter, K., Seagle, C.T., Wang, Y., Prakapenka, V.B., 2009. High pressure effects on the iron-iron oxide and nickel-nickel oxide oxygen fugacity buffers. *Earth and Planetary Science Letters* 286, 556-564.

Irfune, T., Shinmei, T., McCammon, C. A., Miyajima, N., Rubie, D. C., Frost, D. J., 2010. Iron partitioning and density changes of pyrolite in Earth's lower mantle. *Science* 327, 193-195.

Lee, Y.L., Kleis, J., Rossmeisl, J., Morgan, D., 2009. Ab initio energetics of $\text{LaBO}_3(001)$ (B=Mn, Fe, Co, and Ni) for solid oxide fuel cell cathodes. *Phys Rev B* 80.

Lee, Y.L., Morgan, D., 2012. Ab initio and empirical defect modeling of $\text{LaMnO}_{3\pm\delta}$ for solid oxide fuel cell cathodes. *Physical chemistry chemical physics* 14, 290-302.